JℲM PAPERS

Buoyancy instabilities in a liquid layer subjected to an oblique temperature gradient

Ramkarn Patne[1,2,†] **and Alexander Oron**[3]

[1]Department of Chemical Engineering, Indian Institute of Technology (ISM) Dhanbad, Jharkhand 826004, India

[2]Department of Chemical Engineering, Indian Institute of Technology Hyderabad, Kandi, Sangareddy, Telangana 502285, India

[3]Faculty of Mechanical Engineering, Technion – Israel Institute of Technology, Haifa 3200003, Israel

We investigate the temporal and spatio-temporal buoyancy instabilities in a horizontal liquid layer supported by a poorly conducting substrate and subjected to an oblique temperature gradient (OTG) with horizontal and vertical components, denoted as HTG and VTG, respectively. General linear stability analysis (GLSA) reveals a strong stabilizing effect of the HTG on the instabilities introduced by the VTG for Prandtl numbers $Pr > 1$ via inducing an extra vertical temperature gradient opposing the VTG through energy convection. For $Pr < 1$, a new mode of instability arises as a result of a velocity jump in the liquid layer caused by cellular circulation. A long-wave weakly nonlinear evolution equation governing the spatio-temporal dynamics of the temperature perturbations is derived. Spatio-temporal stability analysis reveals the existence of a convectively unstable long-wave regime due to the HTG. Weakly nonlinear stability analysis reveals the supercritical type of bifurcation changing from pitchfork in the presence of a pure VTG to Hopf in the presence of the OTG. Numerical investigation of the spatio-temporal dynamics of the temperature disturbances in the layer in the weakly nonlinear regime reveals the emergence of travelling wave regimes propagating against the direction of the HTG and whose phase speed depends on Pr. In the case of a small but non-zero Biot number, the wavelength of these travelling waves is larger than that of the fastest-growing mode obtained from GLSA.

Key words: buoyancy-driven instability, instability control, absolute/convective instability

† Email address for correspondence: ramkarn@che.iith.ac.in

1. Introduction

Liquid layers subjected to an oblique temperature gradient (OTG) are encountered in geophysical settings (Weber 1978; Ortiz-Pérez & Dávalos-Orozco 2011, 2014), additive manufacturing (Kowal, Davis & Voorhees 2018), material processing and crystal growth (Lappa 2010) and various industrial processes (Kistler & Schweizer 1997). The present investigation is concerned with the understanding of the effect of the horizontal component of the OTG, referred to in what follows as the horizontal temperature gradient (HTG), on the buoyancy instability arising as a result of the vertical component of the OTG, referred to as the vertical temperature gradient (VTG). The present model can be also applicable to partially filled jacketed chemical reactors where the energy is provided/extracted by the liquid circulating in the jacket. The reactor fluid is heated at the bottom wall and the sidewalls by the liquid flowing in the jacket, thereby imposing an OTG. If the fluid flowing in the jacket provides heat energy then it will lead to circulation towards the centre of the reactor from the wall along the interface and in the reverse direction near the bottom and vice versa (Levenspiel 1999). The model considered here mimics the situation in that part of the above system away from the sidewalls.

A liquid layer with a free surface, supported by a solid substrate from below, and subjected to a purely HTG can lead to two types of flows due to thermocapillarity: (i) 'linear flow' possessing a linear profile which is present in an infinitely long liquid layer and (ii) 'return flow' which is present in a rectangular cavity and exhibits a parallel core flow away from the vertical walls of the cavity (Smith & Davis 1983*a*,*b*). These flows arise as a result of the thermocapillary stresses exerted at the free surface which in turn originate from the temperature dependence of the surface tension. The stability of the linear and return flows was explored in detail by Smith & Davis (1983*a*,*b*). Furthermore, the thermocapillary instabilities arising due to an imposed OTG have been also investigated by Nepomnyashchy & Simanovskii (2004), Shklyaev & Nepomnyashchy (2004), Nepomnyashchy & Simanovskii (2009) and Patne, Agnon & Oron (2020*b*, 2021*a*,*b*). Shklyaev & Nepomnyashchy (2004) and Patne *et al.* (2021*a*) revealed a strong stabilizing effect of the imposed HTG component on the instability triggered by the VTG component of the imposed OTG. Additionally, Patne *et al.* (2021*a*) demonstrated the existence of an entirely new class of thermocapillary modes arising as a result of the interaction between the imposed HTG and VTG.

Similarly, a liquid layer confined between two horizontal rigid or free-surface boundaries and subjected to a purely HTG can exhibit a flow as a result of the buoyancy forces termed as Hadley circulation (Hart 1972, 1983). The buoyancy forces arise due to the temperature dependence of the liquid density, which then lead to a circulation. Unlike the linear and return flows caused by thermocapillarity, the buoyancy gives rise to a parallel core flow even in an infinite liquid layer. Hart (1972, 1983) investigated the stability of such flows and found both oscillatory and stationary modes of buoyancy instability due to the imposed HTG in contrast to only stationary modes emerging when the liquid layer is subjected to a purely VTG. Gill (1974) theoretically investigated the stability of Hadley circulation with a focus on liquid metals. Hurle, Jakeman & Johnson (1974) studied experimentally the same problem using molten gallium and validated the theoretical results obtained by Gill (1974). The buoyancy instabilities in a horizontal liquid layer due to the presence of a hot patch creating a HTG were studied by Walton (1985). The nonlinear evolution of the buoyancy instabilities in Hadley circulation was investigated by Kuo & Korpela (1988) and Wang & Korpela (1989). More experimental and numerical studies by Braunsfurth *et al.* (1997), Juel *et al.* (2001) and Hof *et al.* (2004) dealt with a similar problem restricted to molten gallium in greater detail.

The buoyancy instability in a liquid layer constrained between two horizontal rigid boundaries subjected to an OTG was first studied by Weber (1973) for a small HTG. Later, Sweet, Jakeman & Hurle (1977) extended the theory of Weber (1973) to larger values of the imposed HTG, where the mean values of the basic velocity and temperature profiles were specified, while carrying out a stability analysis. Weber (1978) considered the same problem in a liquid layer but now contained between two horizontal stress-free or two rigid, perfectly conducting boundaries. His analysis showed the existence of longitudinal and transverse rolls in addition to oscillatory instability with the dominant mode depending on the Prandtl number. A detailed analysis of the instabilities arising due to an imposed OTG in the same settings was carried out by Nield (1994); however, due to numerical difficulties, his analysis was restricted to Rayleigh numbers below 6000. A detailed analysis of various instability modes in a layer between two horizontal rigid boundaries was recently performed by Ortiz-Pérez & Dávalos-Orozco (2011, 2014). Their analysis revealed the emergence of a new dominant oscillatory oblique mode for Prandtl numbers less than unity.

The previous studies of Weber (1973), Sweet *et al.* (1977), Weber (1978), Nield (1994) and Ortiz-Pérez & Dávalos-Orozco (2011, 2014) dealt with a liquid layer constrained by two horizontal free-surface or two rigid, perfectly conducting boundaries. However, various industrial applications and geophysical flows feature a liquid layer supported by a solid substrate on one side and bounded by a free surface at the other side. Additionally, heat exchange with ambient at the free surface takes place in reality, so the case of an imposed temperature at the gas–liquid interface is rather artificial. The present investigation fills this practically important gap.

Weber (1973), Sweet *et al.* (1977), Weber (1978), Nield (1994) and Ortiz-Pérez & Dávalos-Orozco (2011, 2014) considered only the temporal evolution of disturbances in emerging flows. However, a temporal stability analysis does not provide information about the growth of the disturbances in space or in both space and time simultaneously. This requires a spatio-temporal stability analysis, the instabilities of which may be further classified as either absolute or convective. A convective instability implies that, given sufficient time, the disturbances will decay at any point in space, while an absolute instability leads to the growth of disturbances at any point in space.

A closely related problem is that of a liquid layer subjected to the thermocapillary effect under the action of an OTG. Recent studies by Nepomnyashchy & Simanovskii (2004), Shklyaev & Nepomnyashchy (2004), Nepomnyashchy & Simanovskii (2009) and Patne *et al.* (2020*b*, 2021*a*,*b*) dealing with thermocapillary instabilities alone are relevant to thin liquid layers. The ratio of the Rayleigh and Marangoni numbers is the dynamic Bond number, which is proportional to the second power of the liquid layer thickness; thus an increase in the thickness of the liquid layer favours buoyancy instability. In the present study, we neglect the thermocapillary effect; thus the results are applicable to thicker liquid layers. Below we give an estimate for the lower bound for the layer thickness satisfying several relevant constraints.

The present work investigates the buoyancy instability in a liquid layer with a free non-deformable surface, supported by a poorly conducting planar substrate from below, and subjected to an OTG. Here we carry out both general linear stability analysis (GLSA) and long-wave analysis. We further explore the stabilizing effect of the HTG and the origin of the new instability modes using energy budget analysis and physically supported arguments.

The rest of the paper is arranged as follows. The problem statement, the original governing equations and boundary conditions, the base-state fields and the governing
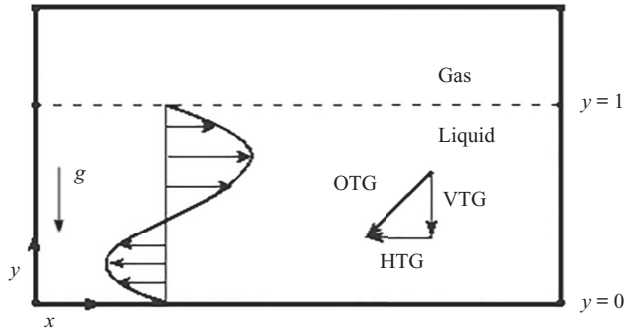
Figure 1. Schematic of the system considered here. The liquid and gas layers are present in a long rectangular container. Both layers are subjected to an OTG with dimensional VTG component $-\beta$ and dimensional HTG component $-\eta^*$, each indicated by an arrow. Such temperature gradients can be imposed by heating the bottom and the left sidewall of the container and/or cooling the top and the right sidewall of the container. The location of the liquid–gas interface at a distance d from the bottom corresponds to $y = 1$ in the sketch.

equations for the evolution of perturbations imposed on the base state are all considered in § 2. The numerical technique employed in resolving the GLSA is briefly outlined in § 3 and its results are presented in § 4. Section 5 is devoted to the energy budget analysis and to the presentation of the physical mechanisms for the stabilization/destabilization of base flow. The linear temporal, spatio-temporal and nonlinear stability analyses in the framework of the long-wave approximation are presented in § 6. The major conclusions of the present investigation are summarized in § 7.

2. Problem formulation

Consider a three-dimensional system that consists of a layer of an incompressible Newtonian liquid of mean thickness d supported from below by a planar solid wall and an inert gas in a long rectangular container with the liquid–gas interface assumed to be non-deformable. The entire system is subjected to an imposed temperature gradient in the gravity field g, as shown in figure 1. The density of the liquid ρ is assumed to linearly depend on temperature, with the rest of the liquid properties, namely dynamic viscosity μ, thermal diffusivity κ and thermal conductivity k_{th}, all being assumed to be independent of temperature. The imposed temperature gradient is assumed to be oblique, i.e. to possess components both parallel and normal to the substrate plane, as illustrated in figure 1. These components of the OTG are referred to as the HTG and VTG, denoted by $-\eta^*$ and $-\beta$, respectively.

The coordinate system used here is Cartesian with the axes x and z located in the substrate plane, whereas the axis y is normal to the substrate and directed into the liquid layer with the reference point $y = 0$ located on the substrate plane. The aspect ratio of the system is assumed to be small $d/L \ll 1$ with L being the length of the container along the x and z axes, thereby allowing for the existence of parallel flow in the core region away from the sidewalls (Smith & Davis 1983a; Mercier & Normand 1996).

The length, time, velocity and temperature are non-dimensionalized by d, d^2/κ, κ/d and βd, respectively, with the value of β to be specified below. Furthermore, the pressure and stresses are scaled by $\mu\kappa/d^2$. Thus, the entire system (the substrate, the liquid layer and the gas phase) is subjected to a constant OTG with the dimensionless VTG component

(-1) in the y direction and the HTG component $(-\eta)$ in the x direction, where

$$\eta = \frac{\eta^*}{\beta}. \tag{2.1}$$

Let the dimensionless fluid velocity field be $\boldsymbol{v} = (v_x, v_y, v_z)$ with v_X being the velocity components in the direction $X = x, y, z$. The dimensionless continuity and momentum conservation equations upon using the Boussinesq approximation are

$$\boldsymbol{\nabla} \cdot \boldsymbol{v} = 0, \tag{2.2a}$$

$$\frac{1}{Pr}[\partial_t \boldsymbol{v} + (\boldsymbol{v} \cdot \boldsymbol{\nabla})\boldsymbol{v}] = -\boldsymbol{\nabla}p + Ra\, T\boldsymbol{\nabla}y + \nabla^2 \boldsymbol{v}, \tag{2.2b}$$

where p and T are the dimensionless pressure and temperature, respectively,

$$Pr = \frac{\mu}{\rho_0 \kappa}, \quad Ra = \frac{\rho_0 g \alpha \beta d^4}{\mu \kappa} \tag{2.2c}$$

are the Prandtl and Rayleigh numbers, $\boldsymbol{\nabla} = (\partial_x, \partial_y, \partial_z)$ is the gradient operator, $\nabla^2 \equiv \partial_x^2 + \partial_y^2 + \partial_z^2$ is the Laplacian operator and ∂_X denotes partial derivative with respect to X. Here, ρ_0 is the density at an arbitrary reference temperature and $\alpha = -1/(\rho_0 (\mathrm{d}\rho/\mathrm{d}T)_p)$ represents the volumetric expansion coefficient of the liquid at constant pressure.

Finally, the dimensionless heat advection–diffusion equation is written as

$$\partial_t T + (\boldsymbol{v} \cdot \boldsymbol{\nabla})T = \nabla^2 T. \tag{2.2d}$$

The governing equations (2.2a)–(2.2d) are subjected to the following boundary conditions. At the solid substrate $y = 0$, these are no-slip (in terms of the x and z components of the velocity field), impermeability and a specified VTG condition:

$$v_x = 0; \quad v_z = 0; \quad v_y = 0; \quad \partial_y T = -1, \tag{2.3a}$$

respectively.

At the gas–liquid interface located at $y = 1$, the boundary conditions are the kinematic boundary condition for a flat and stationary interface, zero stress in the two tangential directions and the continuity of the heat flux:

$$v_y = 0, \tag{2.3b}$$

$$\frac{\partial v_x}{\partial y} + \frac{\partial v_y}{\partial x} = 0, \tag{2.3c}$$

$$\frac{\partial v_z}{\partial y} + \frac{\partial v_y}{\partial z} = 0, \tag{2.3d}$$

$$\boldsymbol{\nabla}T \cdot \boldsymbol{n} = -Bi(T - T_\infty + \eta x), \tag{2.3e}$$

respectively, where $Bi = qd/k_{th}$ is the Biot number. Here, T_∞ and q are the dimensionless temperature at some point of the gas ambient and the coefficient of thermal convection at the free surface, respectively.

Let us now discuss the physical limitations of the current mathematical model. First, the Boussinesq equations are valid when $\alpha \Delta T \ll 1$, where ΔT is a temperature difference

between the bottom and the free surface of the liquid layer along a vertical line. This constraint is equivalent to

$$Ra \ll Ga \equiv \frac{gd^3}{\nu\kappa}, \tag{2.4}$$

where Ga is the Galileo number. Since the values of the Rayleigh number Ra appearing in what follows are below $Ra \leq Ra_m = 10^9$, it follows from (2.4) that the range of validity is

$$d \gg d_1 \equiv \left(\frac{Ra_m\kappa\nu}{g}\right)^{1/3}, \tag{2.5}$$

which in the case of water yields $d \gg 2\,\text{cm}$.

To neglect the thermocapillary effect with respect to the buoyancy effect, the following condition is to be met:

$$Ra \gg Ma \equiv \frac{\gamma\beta d^2}{\nu\kappa}, \tag{2.6}$$

where Ma is the Marangoni number whose definition contains the temperature gradient of surface tension γ. The condition (2.6) yields

$$d \gg d_2 \equiv \left(\frac{\gamma}{\rho_0 g\alpha}\right)^{1/2}, \tag{2.7}$$

which in the case of water leads to $d \gg 1\,\text{cm}$. To combine these two constraints we deduce that the limitation for the forthcoming analysis is that the layer thickness should satisfy the condition $d \gg \max(d_1, d_2)$; thus, for a water layer, it yields $d \gg 2\,\text{cm}$.

2.1. Base state

For the base state assumed to be $\bar{v}_x = \bar{v}_x(y)$, $\bar{v}_y = 0$, $\bar{v}_z = 0$, $\bar{p} = \bar{p}(x, y)$, $\bar{T} = \bar{T}(x, y)$ (note that an overbar denotes hereafter the base state quantities), the governing equations (2.2) are subjected to the following boundary conditions. At the solid substrate $y = 0$:

$$\bar{v}_x = 0; \quad \bar{v}_y = 0; \quad \bar{v}_z = 0; \quad \frac{\partial\bar{T}}{\partial y} = -1; \tag{2.8a}$$

whereas at the flat and stationary (due to mass conservation) gas–liquid interface $y = 1$:

$$\bar{v}_y = 0, \tag{2.8b}$$

$$\frac{\partial\bar{v}_x}{\partial y} = 0, \tag{2.8c}$$

$$\partial_y\bar{T} = -Bi(\bar{T} - T_\infty + \eta x). \tag{2.8d}$$

We also assume the emergence of a cellular flow and require a zero total liquid flow rate at any vertical cross-section of the system:

$$\int_0^1 \bar{v}_x \, \mathrm{d}y = 0. \tag{2.8e}$$

The governing equations (2.2) for a steady and fully developed base-state flow reduce to

$$-\frac{\partial \bar{p}}{\partial x} + \frac{\partial^2 \bar{v}_x}{\partial y^2} = 0, \tag{2.9}$$

$$-\frac{\partial \bar{p}}{\partial y} + Ra\bar{T} = 0, \tag{2.10}$$

$$\frac{\partial^2 \bar{T}}{\partial y^2} = \bar{v}_x \frac{\partial \bar{T}}{\partial x}. \tag{2.11}$$

To obtain the base state, pressure is eliminated from (2.9) and (2.10). This leads to the profiles of the longitudinal velocity component, temperature and pressure in the base state in the form

$$\bar{v}_x = -\frac{\eta Ra}{48}(6y - 15y^2 + 8y^3); \quad \bar{v}_y = 0; \quad \bar{v}_z = 0, \tag{2.12a}$$

$$\bar{T}(x, y) = C_1 - \eta x - y + \frac{\eta^2 Ra\, y^3}{960}(20{-}25y + 8y^2), \tag{2.12b}$$

$$\bar{p} = p_a + Ra \int_0^1 \bar{T}(y)\, \mathrm{d}y, \tag{2.12c}$$

where $C_1 = T_\infty + 1 + \eta^2 Ra/960 + Bi^{-1}$. It is also found using (2.12b) that

$$\beta = \frac{Bi\widetilde{\Delta T}}{(1 + Bi)d}, \tag{2.13}$$

where $\widetilde{\Delta T}$ is the difference between the temperatures of the substrate and the far field along the y axis. Note that the presence of the term Bi^{-1} in the expression for C_1 does not mean that the temperature is high for small Bi, since the temperature is scaled with βd, so Bi cancels out.

It follows from (2.12b) that the HTG induces an additional VTG that modifies the imposed negative VTG expressed by the linear term in y. The higher-order terms in y are also present in $\bar{T}$ and their presence plays a major role in determining the stability of the flow as elaborated in § 4. Furthermore, the induced VTG is proportional to η^2 implying a symmetry with respect to the sign of the imposed HTG.

2.2. *Perturbed state*

Next, infinitesimally small perturbations are imposed on the base state given by (2.12) to carry out the linear stability analysis of the system. Squire's theorem (Schmid & Henningson 2001) is not applicable in the present case due to the symmetry break via the imposed HTG. Thus, in what follows, three-dimensional disturbances are considered.

The governing equations are then linearized around the base state given by (2.12) and normal modes

$$f'(\boldsymbol{x}, t) = \tilde{f}(y)\exp\left[\mathrm{i}(kx + mz - \omega t)\right] \tag{2.14}$$

are substituted into those. Here $f'(\boldsymbol{x}, t)$ is a perturbation to a dynamic quantity $f(\boldsymbol{x}, t)$, such as the components of the fluid velocity field v_x, v_y and v_z, pressure p and temperature T, and $\tilde{f}(y)$ is the corresponding eigenfunction in the Laplace–Fourier space. The parameters k and m are the wavenumbers of the perturbations in the x and z directions, respectively,

and $\omega = \omega_r + i\omega_i$ is the complex frequency. The flow is temporally unstable if at least one eigenvalue satisfies the condition $\omega_i > 0$. For the spatio-temporal stability analysis, both k and ω are complex. The condition for the existence of absolute instability is presented in §6.3.

As a result of this procedure, the linearized continuity, momentum conservation and energy equations become

$$ik\tilde{v}_x + D\tilde{v}_y + im\tilde{v}_z = 0, \tag{2.15a}$$

$$\frac{1}{Pr}\left[-i\omega\tilde{v}_x + ik\bar{v}_x\tilde{v}_x + \tilde{v}_yD\bar{v}_x\right] = -ik\tilde{p} + (D^2 - k^2 - m^2)\tilde{v}_x, \tag{2.15b}$$

$$\frac{1}{Pr}\left[-i\omega\tilde{v}_y + ik\bar{v}_x\tilde{v}_y\right] = -D\tilde{p} + (D^2 - k^2 - m^2)\tilde{v}_y + Ra\,\tilde{T}, \tag{2.15c}$$

$$\frac{1}{Pr}\left[-i\omega\tilde{v}_z + ik\bar{v}_x\tilde{v}_z\right] = -im\tilde{p} + (D^2 - k^2 - m^2)\tilde{v}_z, \tag{2.15d}$$

$$-i\omega\tilde{T} + ik\bar{v}_x\tilde{T} + \partial_x\bar{T}\tilde{v}_x + \partial_y\bar{T}\tilde{v}_y = (D^2 - k^2 - m^2)\tilde{T}, \tag{2.15e}$$

where $D \equiv d/dy$.

Equations (2.15) are then supplemented with the following boundary conditions: at $y = 0$, no slip, no impermeability and a specified temperature gradient at the lower plate imply

$$\tilde{v}_x = 0; \quad \tilde{v}_y = 0; \quad \tilde{v}_z = 0; \quad D\tilde{T} = 0. \tag{2.16a}$$

The boundary conditions at $y = 1$ become

$$\tilde{v}_y = 0, \tag{2.16b}$$

$$ik\tilde{v}_y + D\tilde{v}_x = 0, \tag{2.16c}$$

$$im\tilde{v}_y + D\tilde{v}_z = 0, \tag{2.16d}$$

$$D\tilde{T} + Bi\tilde{T} = 0. \tag{2.16e}$$

Equations (2.15) and (2.16) constitute a generalized linear eigenvalue problem which is to be solved for the eigenvalue ω and the eigenfunctions for a specified set of parameter values Bi, Pr and Ra. To determine the spectrum of the eigenvalue problem (2.15) and (2.16), numerical solution based on the pseudospectral method is carried out.

3. Numerical method

To carry out the linear stability analysis of the problem (2.2)–(2.3e), the pseudospectral method is employed, in which the eigenfunctions corresponding to each dynamic field are expanded into series of the Chebyshev polynomials as

$$\tilde{f}(y) = \sum_{m=0}^{m=N} a_m \mathcal{T}_m(y), \tag{3.1}$$

where $\mathcal{T}_m(y)$ are Chebyshev polynomials of degree m and N is the highest degree of the polynomial in the series expansion or, equivalently, the number of collocation points. The coefficients of the series a_m are the unknowns to be solved for.

The generalized eigenvalue problem is constructed in the form

$$Ae + \omega Be = 0, \tag{3.2}$$

where A and B are matrices obtained from the discretization procedure and e is the vector containing the coefficients of all series expansions.

Further details of the discretization of the governing equations and boundary conditions, and the construction of the matrices A and B are presented in the standard procedure described by Trefethen (2000) and Schmid & Henningson (2001). Application of the pseudospectral method for similar problems can be found in Patne, Agnon & Oron (2020a) and Patne *et al.* (2021a). We use the *polyeig* MATLAB routine to solve the generalized eigenvalue problem given by (3.2). To filter out the spurious modes from the genuine, numerically computed spectrum of the problem, the latter is determined for N and $N + 2$ collocation points, and the eigenvalues are compared with an *a priori* specified tolerance, e.g. 10^{-4}. The genuine eigenvalues are verified by increasing the number of collocation points by 25 and monitoring the variation of the obtained eigenvalues. Whenever the eigenvalue does not change up to a prescribed precision, e.g. to the sixth significant digit, the same number of collocation points is used to determine the critical parameters of the system. In the present work, $N = 50$ is found to be sufficient to achieve convergence and to determine the leading, most unstable eigenvalue within the investigated parameter range.

4. General linear stability analysis

For convenience of the presentation and discussion of the results, the results are subdivided into three separate sections. The first two sections deal with the streamwise instabilities ($m = 0$) for $Pr > 1$ and $Pr < 1$, whereas the third section deals with the spanwise modes ($k = 0$) of instability.

4.1. $Pr > 1$

In the absence of the imposed HTG, i.e. $\eta = 0$, for a poorly conducting substrate, i.e. with a zero heat flux due to temperature perturbations, a long-wave mode of buoyancy or Rayleigh instability is present due to the imposed VTG, hereafter simply referred to as the 'long-wave mode' (Chapman & Proctor 1980; Gertsberg & Sivashinsky 1981). The critical Rayleigh number $Ra_c = 320$ at $Bi = 10^{-5}$ for the present configuration can be analytically obtained as shown in § 6. It must be noted that for a liquid layer bounded by two rigid plates at $y = 0$ and $y = 1$, $Ra_c = 720$ (Gertsberg & Sivashinsky 1981). Since the instability in this case is monotonic, the variation in Prandtl number Pr does not affect Ra_c. A strong stabilizing effect of the increasing strength of the imposed HTG relative to the strength of the imposed VTG denoted by η is shown in figure 2. For $\eta = 0$, the long-wave mode is stationary. However, from figure 2, the imposed HTG not only stabilizes the long-wave mode but also makes it an oscillatory mode travelling against the HTG direction since $\omega_r > 0$. The stabilizing effect of an increase in η on the long-wave mode is also illustrated by the neutral stability curves shown in figure 3.

In the companion problem of a liquid layer subjected to an OTG and thermocapillarity (Patne *et al.* 2021a), a new mode of the thermocapillary instability was demonstrated to exist. This mode arises as a result of an interaction between the imposed HTG and VTG, while the long-wave thermocapillary mode driven by the imposed VTG is stabilized due to the imposed HTG. Figure 3 shows that similar to the thermocapillary long-wave mode, the imposed HTG has a strong stabilizing effect on the long-wave buoyancy mode too. However, unlike the thermocapillary problem, here, a new mode does not arise with an increase in η as illustrated in figure 3.

The stabilization of the long-wave mode due to the imposed HTG leads to the formation of an island of instability in the η–Ra_c plane as illustrated for $Pr = 10$ in figure 4. It must be noted that a liquid layer subjected to a HTG also exhibits buoyancy instability in addition to the thermocapillary instability (Mercier & Normand 1996). However, as
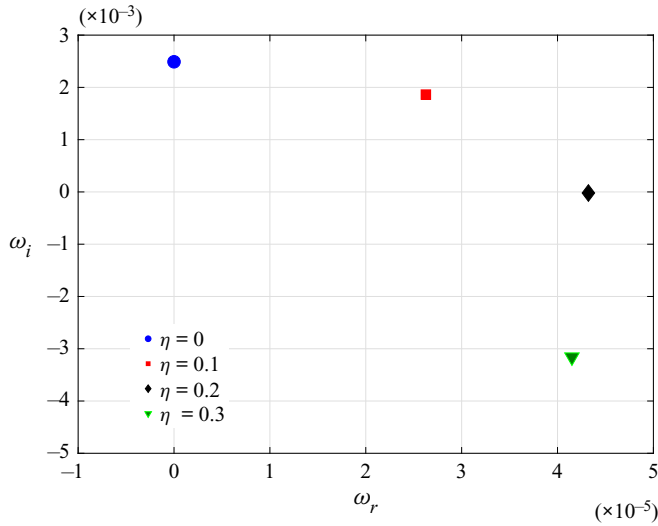
Figure 2. Variation of the long-wave mode with η in the ω_r–ω_i space at $Bi = 10^{-5}$, $m = 0$, $k = 0.1$, $Ra = 400$ and $Pr = 10$. The figure illustrates the stabilization and transformation of the long-wave mode from monotonic at $\eta = 0$ into oscillatory with an increase in η.
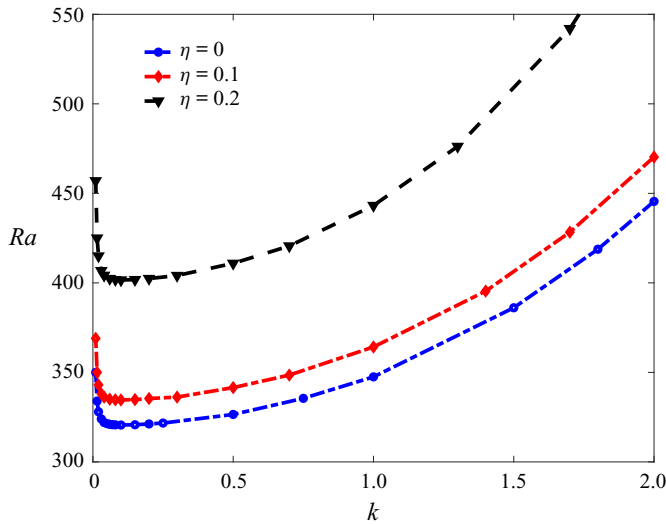

Figure 3. Neutral stability curves ($\omega_i = 0$) in the Ra–k space at $Pr = 10$ and $Bi = 10^{-5}$ for several values of η. The figure confirms the stabilizing effect of an increase in η on the long-wave mode.

follows from figure 4, for $\eta > 0.25$, the liquid layer is linearly stable with respect to the buoyancy instabilities. Unlike thermocapillary instability investigated by Patne *et al.* (2021*a*) at high η, there is an absence of the unstable mode of buoyancy instability due to the imposed HTG. Thus, the VTG also has a strong stabilizing effect on the buoyancy instability introduced by the imposed HTG. The island of instability depicted in figure 4 for $Pr = 10$ slightly shifts towards higher Ra_c for $Pr = 1000$, showing a weak effect of the variation in Pr. It must be noted that independently of η, the critical wavenumber is $k_c \sim 0.1$, implying that the mode of instability remains a long-wave mode.
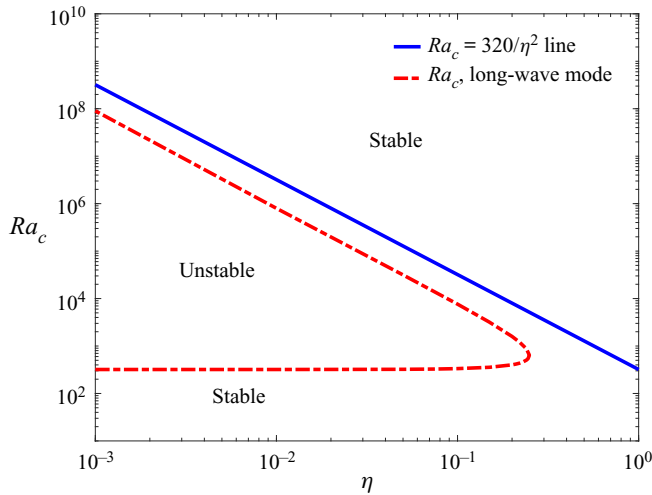
937 A11-10

Figure 4. Variation of the critical Rayleigh number Ra_c with the dimensionless strength of the HTG η at $Pr = 10$, $m = 0$ and $Bi = 10^{-5}$. The long-wave mode driven by the VTG forms an island of instability constrained to $\eta < 0.25$. Unlike in the low-Pr case discussed in § 4.2, the new mode of instability is absent for high Pr, thus providing an avenue for a complete suppression of the buoyancy instability. The island of instability is negligibly affected with a further increase in Pr. The upper bound on the stability island is the asymptote $Ra_c = 320/\eta^2$, which is deduced, see (4.1), directly from the base-state temperature gradient.

The upper Ra_c boundary of the instability island shown in figure 4 represents in fact that the stabilization boundary exhibits scaling of $Ra_c \sim 1/\eta^2$ for $\eta \ll 1$, which is deduced directly from the expression for the induced temperature component given by the quintic polynomial in the base-state temperature as appears in (2.12b). The line $Ra = 320/\eta^2$ represents a line along which the average VTG obtained by integrating (2.12b) across the layer $y \in [0, 1]$, and equating the result to zero:

$$\frac{\eta^2 Ra}{320} - 1 = 0 \Rightarrow Ra = \frac{320}{\eta^2}. \tag{4.1}$$

To reiterate, this asymptotic line is a result of the balance between the imposed VTG and the induced VTG. The induced VTG, which arises due to the imposed HTG, is positive, whereas the imposed VTG is negative. Hence the induced VTG opposes the imposed VTG, thereby stabilizing the long-wave mode driven by the imposed VTG. Therefore, the imposed HTG is responsible for the stabilization of the long-wave mode via the induced VTG. A further observation of figure 5 shows that for a sufficiently high Bi, the upper branch of the curve can cross the line $Ra_c = 320/\eta^2$. This feature implies that although the average VTG for the base flow becomes positive, a locally negative temperature gradient near the substrate with sufficiently high, but still small, Biot number may still produce an instability.

The effect of variation in Bi on the critical parameters is presented in figure 5. An increase in Bi from 10^{-5} to 0.1 leads to a slight shift in the lower boundary of the island of instability to a higher Ra_c implying a stabilizing effect. The upper boundary, which displays a scaling $Ra_c \sim 1/\eta^2$, also shifts to a higher Ra_c leading to a broadening of the Ra_c range for the island of instability. It must be noted that for the entire range of η, the critical wavenumber $k_c \sim 1$ and $k_c = 0.1$ for the $Bi = 0.1$ and $Bi = 10^{-5}$ cases, respectively. Therefore, k_c remains invariant with respect to variation in η.
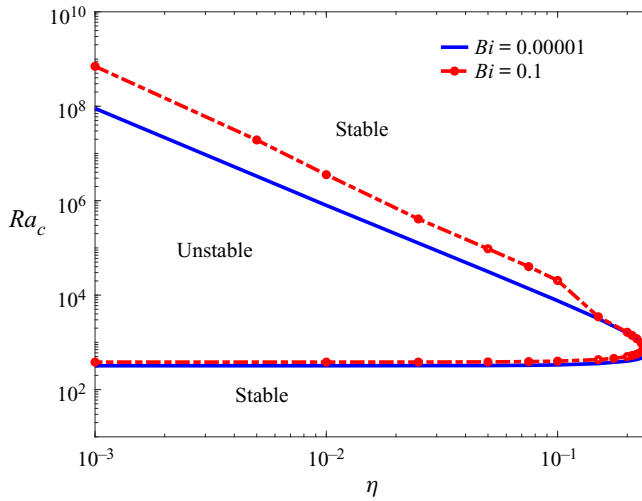
Figure 5. Variation of Ra_c with η at $Pr = 10$ and $m = 0$. An increase in Bi causes a shift of the island boundaries towards higher values of Ra_c, which effectively leads to a broadening of the instability island in terms of Ra_c for $Bi = 0.1$, as compared with the $Bi = 10^{-5}$ case.

An important remark is now in order. The dynamic Bond number, i.e. the ratio of the Rayleigh and Marangoni numbers Ra/Ma, is proportional to d^2; thus for an increase in the thickness of the liquid layer, the buoyancy instability will dominate over the thermocapillary instability. However, the buoyancy instabilities are absent for $\eta > 0.25$, while the thermocapillary instabilities are present (Patne *et al.* 2021*a*); thus even for thicker liquid layers the Marangoni instability will be present. This conclusion provides an interesting avenue to experimentally observe the thermocapillary instability even in the case of thick liquid layers subjected to an OTG.

4.2. $Pr < 1$

The absence of buoyancy instability for $\eta > 0.25$, as discussed in §4.1 for $Pr > 1$, does not hold true for $Pr < 1$. Figure 6 shows that the long-wave mode is stabilized by the induced VTG with an increase in η in the range $\eta < 0.1$. However, for $\eta > 0.1$, a new finite-wavenumber mode with $k_c \neq 0$ emerges, henceforth simply referred to as a 'new mode'. For $\eta > 0.1$, Ra_c of the long-wave mode starts a rapid increase to reach a maximum at $\eta \sim 0.2$, while k_c deviates from 0 to undergo a rapid growth to reach its maximum at $\eta \sim 0.15$. A further increase in η leads to a fast decrease in both k_c and Ra_c, but for $\eta > 1$, k_c tends to a constant value ~ 0.88. However, Ra_c continues to decrease with an increase in η and exhibits a characteristic scaling $Ra_c \sim 1/\eta$ for $\eta > 1$.

It is interesting to note that a liquid layer subjected to an OTG exhibits a new mode of thermocapillary instability for high η and the critical Marangoni number Ma_c exhibits a scaling $Ma_c \sim 1/\eta$ (Patne *et al.* 2021*a*), similar to that of Ra_c in the present study. Thus, for $Pr < 1$, the buoyancy instability exhibits characteristics similar to those of the thermocapillary instability.

At very low Pr, the stability picture presented for $Pr = 0.1$ in figure 6 undergoes further modification. For $Pr = 0.001$ (see figure 7*b*), the long-wave mode forms an instability island similar to the case for $Pr > 1$, but the new mode is also present. The latter bifurcates from the long-wave curve at $\eta \sim 0.005$. The neutral stability curves shown in figure 7(*a*)
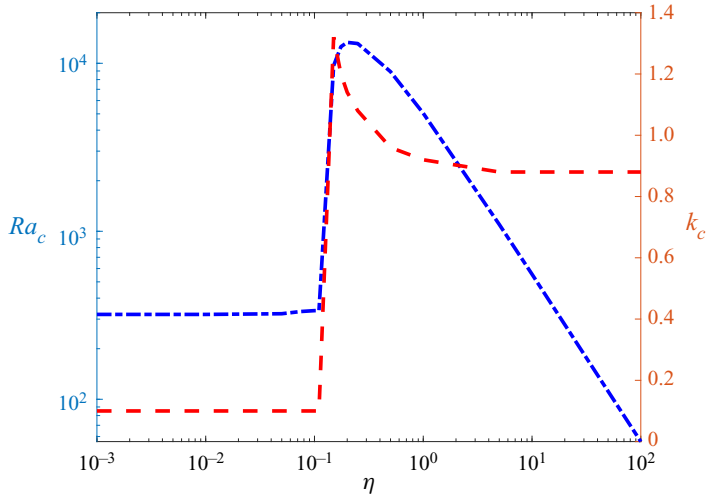
Figure 6. Variation of Ra_c and k_c with η at $Pr = 0.1$, $m = 0$ and $Bi = 10^{-5}$. The base-state flow is unstable for $Ra > Ra_c$. At $\eta > 0.15$, the unstable long-wave mode switches to a new mode. The new mode results from an interaction of the imposed HTG and VTG, and shows a characteristic scaling $Ra \sim 1/\eta$ for $\eta > 1$.
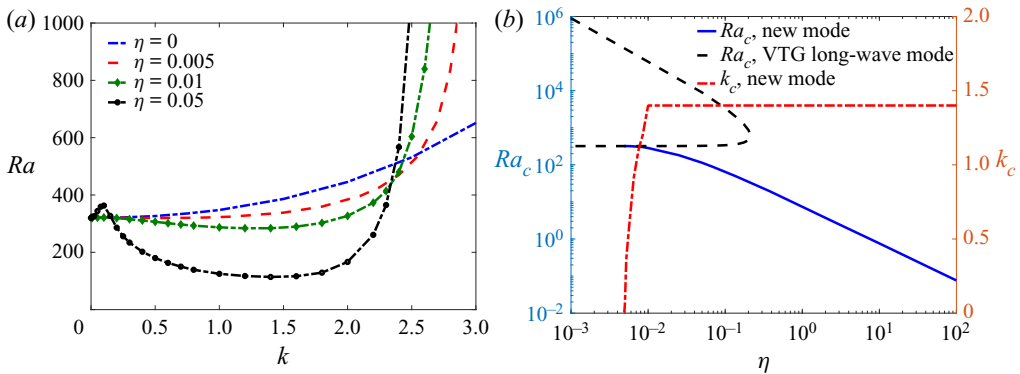

Figure 7. (*a*) Neutral stability curves. The formation of two minima is observed with an increase in η showing the origin of the new mode from the long-wave mode. (*b*) Variation of Ra_c and k_c with η at $Pr = 0.001$, $m = 0$ and $Bi = 10^{-5}$. The long-wave mode driven by the imposed VTG creates an island of instability constrained to $\eta < 0.1$. At $\eta \sim 0.005$, the long-wave mode gives rise to a new finite-wavenumber mode which becomes the most unstable mode at higher η. Similar to the case of $Pr = 0.1$, the new mode displays a characteristic scaling $Ra_c \sim 1/\eta$ for $\eta > 0.1$. The curve for k_c of the new mode shows a rapid increase from 0 when the new mode separates from the long-wave mode to a constant value ~ 1.4 at high η.

illustrate the origin of the emergence of the new mode from the long-wave mode. At $\eta = 0$, the neutral stability curve is the same as that for $Pr = 10$, as presented in figure 3. However, as η increases, the neutral stability curve tends to form a minimum at $k \neq 0$, as observed in figure 7(*a*) for $\eta = 0.005$ and $\eta = 0.01$, thereby illustrating the signs of formation of the new mode. Eventually, for $\eta = 0.05$ the long-wave mode exhibits two clear minima, one at $k = 0$ corresponding to the long-wave mode and the other at $k \sim 1.4$ corresponding to the new finite-wavelength mode.

Returning to figure 7(*b*), the critical wavenumber k_c for the new mode rapidly increases from 0 and reaches a constant value ~ 1.4 at $\eta \sim 0.01$. Observation of figures 6 and 7(*b*)
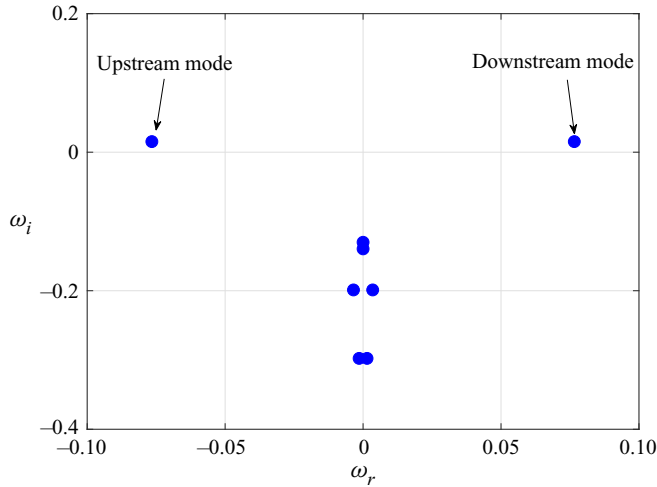
Figure 8. The unstable spanwise mode pair in the eigenspectrum of the problem at $Pr = 0.001$, $k = 0$, $m = 0.3$, $Ra = 55$, $\eta = 1$ and $Bi = 10^{-5}$. These modes become unstable for $Pr < 1$ and possess the same growth rate travelling in the opposite directions with the same phase speed.

shows that as Pr increases, the new mode shifts towards higher Ra_c, eventually leading to a complete stabilization for $Pr > 1$. It is emphasized that liquid metals, owing to their high thermal conductivity, satisfy the condition of $Pr \sim 0.001$–0.1. Thus, the new mode revealed here, in principle, may be experimentally observed in liquid metal layers subjected to an OTG, which also illustrates the practical significance of the present study.

4.3. *Spanwise mode* ($k = 0$)

The analysis for the spanwise mode shows that the imposed HTG has a stabilizing effect on the spanwise long-wave mode similar to that for the streamwise long-wave mode for $Pr > 1$. In fact, the spanwise long-wave mode forms an island of instability exactly the same as the curve shown in figure 4 for the streamwise long-wave mode. For the sake of brevity, we do not present the corresponding curve for the spanwise long-wave mode.

Similar to the new mode revealed for $Pr < 1$, the spanwise new modes of instability also exist with one difference, namely, while the streamwise perturbations exhibit a single new mode of instability, the spanwise perturbations consist of a pair of new modes possessing the same growth rate ω_i, with one of them travelling in the positive z direction, whereas the other one propagates in the negative z direction with the same phase speed, as shown in figure 8. Here, we refer to the modes travelling in the positive and negative z direction as downstream and upstream modes, respectively. These modes possess considerably higher values of Ra_c than the streamwise new mode discussed in § 4.2. For example, at $\eta = 0.1$, for the streamwise mode the critical Rayleigh number is $Ra_c \sim 65$, whereas for the spanwise unstable pair it is $Ra_c \sim 140$. Therefore, the spanwise new modes may not be of much relevance to the present problem, and they are not analysed in detail below. It must be noted that these modes are purely spanwise, i.e. an increase of the streamwise wavenumber k leads to a strong stabilization of these modes.

5. Energy budget analysis and physical mechanism

5.1. *Energy budget analysis*

To understand the origins of the new mode of instability emerging for $Pr < 1$, we carry out an energy budget analysis for the case of two-dimensional ($m = 0$) perturbations and follow the approach used by Hu, He & Chen (2016), Hu *et al.* (2017) and Patne *et al.* (2021*a*).

First, the Navier–Stokes equations in the Boussinesq approximation (2.2*b*) are linearized around the base state $\bar{\boldsymbol{v}}, \bar{p}, \bar{T}$, and recast in the form

$$\frac{1}{Pr}\frac{\partial \boldsymbol{v}'}{\partial t} = -\nabla p' + \nabla \cdot \boldsymbol{\tau}' + Ra\, T' \nabla y - \frac{1}{Pr}\left[(\boldsymbol{v}' \cdot \nabla)\bar{\boldsymbol{v}} + (\bar{\boldsymbol{v}} \cdot \nabla)\boldsymbol{v}'\right], \qquad (5.1)$$

where $\boldsymbol{\tau}'$ is the disturbance of the stress tensor for a Newtonian fluid. Taking the scalar product of (5.1) with the perturbation velocity vector $\boldsymbol{v}'$, integrating the result over the flow domain and simplifying the resulting integrals yields an equation describing the time evolution of the total kinetic energy of the perturbations,

$$E = \frac{1}{2}\int \boldsymbol{v}' \cdot \boldsymbol{v}'\, \mathrm{d}V, \qquad (5.2)$$

in the form

$$\frac{1}{Pr}\frac{\partial E}{\partial t} = -\frac{1}{2}\int \boldsymbol{\tau}' : \dot{\boldsymbol{\gamma}}'\, \mathrm{d}V + Ra\int T' v_y'\, \mathrm{d}V - \frac{1}{Pr}\int \boldsymbol{v}' \cdot \bar{\dot{\boldsymbol{\gamma}}} \cdot \boldsymbol{v}'\, \mathrm{d}V$$

$$\equiv -I_b + I_{RB} - I_R, \qquad (5.3)$$

where I_b, I_{RB} and I_R are the bulk stress work, Rayleigh–Bénard integral or buoyancy work and the Reynolds stress work (Drazin 2002) in the energy balance, respectively, $\mathrm{d}V$ is the volume element and $\dot{\boldsymbol{\gamma}}' = \nabla \boldsymbol{v}' + \nabla \boldsymbol{v}'^{\mathrm{T}}$ and $\bar{\dot{\boldsymbol{\gamma}}} = \nabla \bar{\boldsymbol{v}} + \nabla \bar{\boldsymbol{v}}^{\mathrm{T}}$ represent the strain-rate tensors associated with the perturbed and base states, respectively.

Since the perturbations of the normal component of the velocity field $\boldsymbol{v}'$ vanish at both non-deformable interfaces, namely the free interface $y = 1$ and the liquid–solid interface $y = 0$, the pressure work term in the energy balance equation (5.3) containing area integrals evaluated at these two interfaces vanishes, and thus is not presented there explicitly. Therefore, unlike the energy budget in the case of thermocapillary instability (Patne *et al.* 2021*a*), the pressure work does not contribute here. Some sample values of the various terms in (5.3) are shown in table 1. The buoyancy work term I_{RB} in (5.3) is found to be positive for the parameter values explored here; thus it exerts a destabilizing effect. The bulk stress work component I_b is unconditionally positive in the case of a Newtonian fluid, since $\boldsymbol{\tau}' : \dot{\boldsymbol{\gamma}}' = \gamma_{ij}'\gamma_{ji}' \geq 0$, and thus leads to a decrease in the perturbation energy expressing the presence of viscous dissipation. Note that the long-wave mode for $\eta = 0$ may emerge even if the bulk stress work integral is positive. These long-wave modes may become unstable due to the energy supplied by the buoyancy work I_{RB} that overcomes the stabilizing impact of the dissipation factors such as viscous forces and thermal diffusion of the energy.

The Reynolds stress work I_R in the energy balance equation (5.3) represents a volume-averaged correlation between the perturbations in the horizontal and vertical components of the velocity field. This term is also responsible for the energy exchange between the base state and the perturbation fields. It must be noted that I_R is found to be negative for the parameter range studied here. The role of the Reynolds stress work

R. Patne and A. Oron

Parameters	I_b	I_R
$k = 0.01,\ Ra = 400,\ \eta = 0$	0.00015	0
$k = 1.4,\ Ra = 400,\ \eta = 0.01$	0.12282	-1.39266
$k = 1.4,\ Ra = 60,\ \eta = 10$	0.208261	-365.186

Table 1. Sample values of the bulk stress work I_b and Reynolds stress work I_R components in the energy balance equation (5.3) normalized by the value of the buoyancy work I_{RB} for $Bi = 0.001, m = 0$ and $Pr = 0.001$ in the case of the unstable stationary long-wave mode (the first row) and the new modes (the last two rows). The bulk stress work remains positive as expected, and hence has a stabilizing effect driven by the viscous dissipation. The Reynolds stress work is negative and increases rapidly with an increase in η, which results in the growth of the perturbation energy. Therefore, the main source of destabilization for the new mode is the Reynolds stress work.

is enhanced at low values of Pr and high values of η. It follows from table 1 where all values of the integrals are normalized with respect to the buoyancy work term I_{RB}, that the contribution of the latter to the energy balance is the main source of the perturbation energy for the long-wave mode, as seen in the first row of table 1. However, as follows from the last two rows of table 1, the contribution of the buoyancy work term I_{RB} to the perturbation energy for the new mode becomes less important with an increase in η.

As shown in figure 7(b), the new mode bifurcates from the long-wave mode at $\eta \sim 0.005$ and table 1 illustrates that the Reynolds stress work and the buoyancy work are of comparable magnitudes for $\eta = 0.01$. Thus, the buoyancy work also significantly contributes to the destabilization of the new mode in the low-η domain, but its influence diminishes with an increase in η. To conclude, the major sources of the perturbation energy for the long-wave and the new modes are the buoyancy work and the Reynolds stress work, respectively. However, the emergence of the new modes for $Pr < 1$ is associated with the rise in the Reynolds stress work.

It must be noted that the perturbation energy analysis carried out here can only provide an idea about perturbation energy sources that may lead to destabilization (Drazin 2002). However, the right critical parameter values may be obtained only using the GLSA.

5.2. Physical mechanism

The physical mechanism responsible for the onset of buoyancy-driven or Rayleigh–Bénard convection in a liquid layer subjected to a purely VTG is well understood. Given that the substrate is at a higher temperature compared to the liquid–gas interface, a negative VTG is imposed across the layer. Consider a liquid parcel located at $y = y_0$. Due to the imposed VTG, the density of the liquid parcel located at $y = y_0$ will be lower compared with that of the liquid layer present at $y = y_0 + \Delta y$, where $\Delta y > 0$ is a small quantity. In the presence of the gravity field, the liquid parcel will thus try to move to $y = y_0 + \Delta y$. Such a motion will be opposed by the dissipative effects such as viscosity and thermal diffusion of the liquid, but if the VTG strength is sufficiently strong, then the parcel can overcome the dissipative effects combined and succeed in moving to $y = y_0 + \Delta y$ owing to the buoyancy forces, thereby setting in the buoyancy-driven instability. Having understood the physical mechanism of the buoyancy-driven instability caused by the purely imposed VTG, we now proceed to understand the effect of the imposed HTG on the VTG-induced convection and the origin of the new mode of instability.

937 A11-16
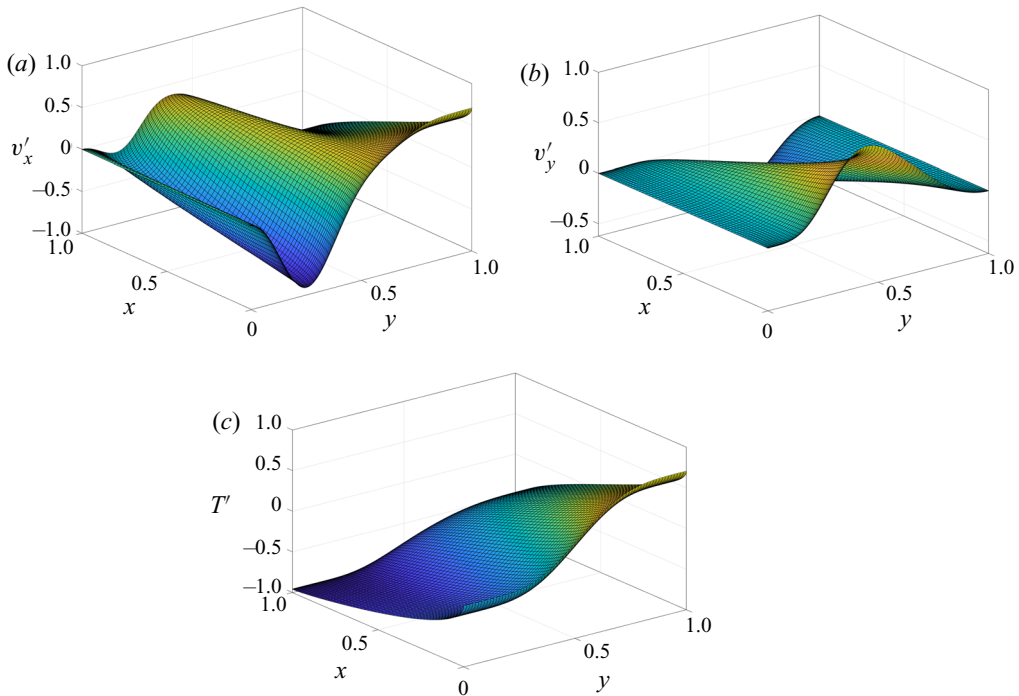
Figure 9. Normalized perturbation fields for $Bi = 10^{-5}, Pr = 0.001, \eta = 1, Ra = 7.5, m = 0$ and $k = 0.38$ for the marginally stable eigenvalue $\omega = 0.055044$. Here, (a) $v'_x = Re[\tilde{v}_x\, e^{ikx}]$, (b) $v'_y = Re[\tilde{v}_y\, e^{ikx}]$ and (c) $T' = Re[\tilde{T}\, e^{ikx}]$. The length of the domain in the x direction is equal to the wavelength of the perturbations $2\pi/k$. For convenience, the axes are normalized to the interval [0, 1]. The normal velocity perturbation field (b) exhibits the maximal variation in the layer and vanishes at both boundaries providing a hint for the destabilization mechanism of the new mode.

5.2.1. *Long-wave mode stabilization*

In §4, we illustrated the strong stabilizing effect of the imposed HTG on the long-wave mode introduced by the imposed VTG. The physical consequences of such stabilization can be understood as follows. It is inferred from (2.12b) that along with the imposed VTG, the latter also gives rise to an induced VTG which has a quartic polynomial form in y. The average total VTG defined as $\langle \bar{T}_y \rangle \equiv \int_0^1 (\partial \bar{T}/\partial y)\, dy$ is thus

$$\langle \bar{T}_y \rangle = \frac{\eta^2 Ra}{320} - 1, \qquad (5.4)$$

which shows that the induced VTG being positive always opposes the imposed VTG.

As discussed in the previous section, for the buoyancy instability to set in the buoyancy forces must overcome the viscous forces and thermal diffusion of the energy. However, the induced VTG opposes the imposed VTG, which leads to the weakening in the total VTG. The buoyancy force caused by the weakened VTG may not be sufficient to overcome the viscous forces and thermal diffusion of the energy which then leads to the predicted stabilization with an increase in Ra. When the vertically averaged imposed and induced VTGs are of equal magnitude, the average VTG vanishes, which yields the relationship $Ra = 320/\eta^2$, thereby defining the upper bound on the threshold of the long-wave instability, which turns out to be valid for very low values of the Biot number Bi, as indeed shown in the case presented in figure 4. However, for higher but still low

values of *Bi*, the instability may still exist for a positive averaged total VTG, as shown in figure 5.

5.2.2. *New mode*

As discussed in § 5, the maximal contribution to the perturbation energy for the new mode arises from the Reynolds stress work which involves a $1/Pr$ term. Thus, with a decrease in *Pr*, the contribution of the Reynolds stress work increases with a further destabilization of the base flow. A decrease in *Pr* implies an enhancement of the inertial effects as seen from (5.1). Additionally, the condition of $Pr < 1$ for the emergence of the new mode emphasizes the major role of inertia. The normalized perturbation fields for the new mode are shown in figure 9. The temperature perturbation field exhibits variation through the entire liquid layer; however, the normal velocity perturbation exhibits the maximal variation evaluated by the absolute value of the gradient vector at $y \sim 0.578$ and vanishes at both ends. The base-state velocity $\bar{v}_x$ vanishes at $y \sim 0.578$ being positive for $y > 0.578$ and negative for $y < 0.578$; therefore there exists a static layer arising as a result of the opposing shear stresses exerted by the forward ($\bar{v}_x > 0$) and return ($\bar{v}_x < 0$) flows. As a result, there exists a velocity jump over a thin layer at $y \sim 0.578$, which is known to be responsible for various kinds of instabilities (Hinch 1984). Here, such a jump could result in the emergence of the new mode of instability provided that the inertial effects are sufficiently strong. To conclude, the new mode of instability revealed here may emerge as a result of the velocity jump in the liquid layer.

6. Long-wave analysis

In this section, we carry out the long-wave analysis of the system. In particular, we derive a weakly nonlinear evolution equation governing the spatio-temporal dynamics of the liquid layer in the limit of a small Biot number following the approach of Chapman & Proctor (1980), Gertsberg & Sivashinsky (1981) and Oron & Nepomnyashchy (2004). Based on the evolution equation derived here, we perform linear stability analysis, both temporal and spatio-temporal, weakly nonlinear analysis to elucidate the type of bifurcation from the equilibrium and finally we numerically investigate the nonlinear dynamics of the system in the framework of the aforementioned evolution equation.

In what follows, we restrict our analysis to that of two-dimensional dynamics. Although it is possible to extend the derivation of the evolution equation and the linear and weakly nonlinear analyses to the three-dimensional case, it is impossible to numerically investigate the nonlinear dynamics of the system in three dimensions, even only due to very large times needed to be reached for the system to attain its saturated state.

6.1. *Derivation of the evolution equation*

In the governing equations (2.2), the dependent variables are expressed as $v_x = \bar{v}_x + v'_x$, $v_y = v'_y$, $p = \bar{p} + p'$ and $T = \bar{T} + T'$ to obtain the equations in terms of the deviations from the base state:

$$\partial_x v'_x + \partial_y v'_y = 0, \tag{6.1a}$$

$$\frac{1}{Pr}\left[\partial_t v'_x + (\bar{v}_x + v'_x)\partial_x v'_x + v'_y\partial_y(\bar{v}_x + v'_x)\right] = -\partial_x p' + (\partial_x^2 + \partial_y^2)v'_x, \tag{6.1b}$$

$$\frac{1}{Pr}\left[\partial_t v'_y + (\bar{v}_x + v'_x)\partial_x v'_y + v'_y \partial_y v'_y\right] = -\partial_y p' + (\partial_x^2 + \partial_y^2)v'_y + RaT', \qquad (6.1c)$$

$$\partial_t T' + (\bar{v}_x + v'_x)\partial_x T' + v'_y \partial_y (\bar{T} + T') = (\partial_x^2 + \partial_y^2)T', \qquad (6.1d)$$

where the dependent variables with primes represent the above-mentioned respective deviations. Similarly, the boundary conditions (2.3e) are modified to read: at $y = 0$, no slip, no impermeability and a specified temperature gradient at the lower plate imply

$$v'_x = 0; \quad v'_y = 0; \quad v'_z = 0; \quad \partial_y T' = 0. \qquad (6.2a)$$

At $y = 1$, the kinematic boundary condition, zero tangential stress and the heat transfer condition become

$$v'_y = 0, \qquad (6.2b)$$

$$\partial_x v'_y + \partial_y v'_x = 0, \qquad (6.2c)$$

$$\partial_y T' + Bi\, T' = 0. \qquad (6.2d)$$

The deviation velocities are further expressed via the streamfunction ψ using the relations

$$v'_x = \partial_y \psi; \quad v'_y = -\partial_x \psi. \qquad (6.3a,b)$$

As noted above, we assume small values of η, $\eta = \epsilon \hat{\eta}$, so that $\hat{\eta} = O(1)$ and $\epsilon \ll 1$ is a smallness scale of η used hereafter as a small expansion parameter in the asymptotic analysis. The following scaling is applied:

$$\xi = \epsilon x; \quad \tau = \epsilon^4 t; \quad \psi = \epsilon \hat{\psi}; \quad T' = \hat{T}; \quad Bi = \epsilon^4 \widehat{Bi}, \qquad (6.4a\text{–}e)$$

with a hat used to denote a scaled value. Equations (6.4a–e) are then substituted into the governing equations (6.1) and the boundary conditions (6.2), the pressure field is eliminated from the equations and these are modified using (6.3a,b). Furthermore, the scaled streamfunction, the temperature and the Rayleigh number are expanded as

$$\hat{\psi} = \psi_0 + \epsilon^2 \psi_2 + \epsilon^4 \psi_4 + \cdots, \qquad (6.5a)$$

$$\hat{T} = T_0 + \epsilon^2 T_2 + \epsilon^4 T_4 + \cdots, \qquad (6.5b)$$

$$Ra = Ra_0 + \epsilon^2 \widehat{Ra_2} + \epsilon^4 \widehat{Ra_4} + \cdots. \qquad (6.5c)$$

Following elimination of pressure, (6.1) are rewritten along with (6.5) to yield at zero-order approximation in ϵ

$$\partial_y^4 \psi_0 + Ra_0 \partial_\xi T_0 = 0; \quad \partial_y^2 T_0 = 0. \qquad (6.6a,b)$$

The boundary conditions are similarly simplified. Given the linear form of the boundary conditions in the present problem, for the sake of brevity, we do not write out the boundary conditions in the following analysis since they are readily obtained from (6.2) by substituting expansions (6.5).

Equations (6.6a,b) admit the solution for ψ_0 and T_0 in the form

$$T_0 = F(\xi, \tau); \quad \psi_0 = \frac{Ra_0}{48}(3y^2 - 5y^3 + 2y^4)\partial_\xi F, \qquad (6.7a,b)$$

where $F(\xi, \tau)$ is an unknown function at this stage whose governing evolution equation is now being derived to determine the spatio-temporal dynamics of the system.

We remind the reader that F represents the leading order in ϵ perturbation of the base-state temperature field.

Similarly, the bulk equations (6.1) at $O(\epsilon^2)$ read

$$- 48Pr\partial_y^4\psi_2 + 6\hat{\eta}Ra_0(8y - 5)\partial_\xi\psi_0 + 48Pr\,\widehat{Ra_2}(\partial_\xi F + \partial_\xi T_2)$$

$$+ \hat{\eta}Ra_0 y(-6 + 15y - 8y^2)\partial_\xi\partial_y^2\psi_0 - 96Pr\partial_\xi^2\partial_y^2\psi_0 = 0, \tag{6.8a}$$

$$\partial_y^2 T_2 + \partial_\xi^2 F - \partial_\xi\psi_0 + -\partial_\xi F\partial_y\psi_0$$

$$+ \hat{\eta}Ra_0\left(\frac{1}{8}y - \frac{5}{16}y^2 + \frac{1}{6}y^3\right)\partial_\xi F = 0. \tag{6.8b}$$

Using the appropriate boundary conditions at $O(\epsilon^2)$, the above equations are then solved.

To obtain the value for Ra_0, (6.8b) is integrated with respect to y across the layer $y \in (0, 1)$ using the boundary conditions at $O(\epsilon^2)$. The resulting equation is then solved for Ra_0 to yield $Ra_0 = 320$, which is in excellent agreement with $Ra_c = 320$ obtained from the numerical solution for a liquid layer subjected to a purely VTG in § 4, thereby validating the accuracy of the numerical approach. Also note that Gertsberg & Sivashinsky (1981) find that in the case of a layer bounded by two solid walls, $Ra_c = 720$. A lower value of the critical Rayleigh number Ra_c here is due to the fact that the case of solid wall-free surface features less dissipation in the presence of one solid boundary, as compared to the case of a layer bounded by two solid walls. Therefore, the system needs a lower value for Ra for instability to set in.

The solution of (6.8) satisfying the appropriate boundary conditions at second order in ϵ is

$$\psi_2 = \frac{y^2}{9072Pr}(Pr\partial_\xi F(189\widehat{Ra_2}(y - 1)(2y - 3)$$

$$+ 320(435 - 505y + 2y^5(72 - 45y + 8y^2))\partial_\xi^2 F)$$

$$+ 32(1890Pr(-1 + y)(-3 + 2y)\partial_\xi G - 5\hat{\eta}(177 - 347y$$

$$+ 2Pr(435 - 505y + 2y^5(72 - 45y + 8y^2))$$

$$+ 2y^3(378 - 630y + 522y^2 - 225y^3 + 40y^4))\partial_\xi^2 F$$

$$+ Pr(90 + y(240 - 945y + 945y^2 - 378y^3 + 90y^5 - 50y^6 + 8y^7))\partial_\xi^3 F)), \tag{6.9a}$$

$$T_2 = G(\xi, \tau) - \frac{6y^3}{18}(20 - 25y + 8y^2)(2\hat{\eta} - \partial_\xi F)\partial_\xi F$$

$$+ \frac{y^2}{18}(8y^6 - 30y^5 + 30y^4 - 9y^2)\partial_\xi^2 F, \tag{6.9b}$$

where $G(\xi, \tau)$ is an unknown function, which turns out to be irrelevant for the evolution of the system up to $O(\epsilon^4)$.

At $O(\epsilon^4)$, the energy equation reads as

$$- \partial_\tau F + \hat{\eta}\partial_y\psi_2 + \partial_y^4 T_2 + 20\hat{\eta}^2 y^2\partial_\xi\psi_0 - \frac{100}{3}\hat{\eta}^2 y^3\partial_\xi\psi_0$$

$$+ \frac{40}{3}\hat{\eta}^2 y^4\partial_\xi\psi_0 + \partial_y T_2\partial_\xi\psi_0 - \partial_\xi\psi_2 + \frac{1}{8}\hat{\eta}\widehat{Ra_2}y\partial_\xi F$$

$$- \frac{5}{16}\hat{\eta}\widehat{Ra_2}y^2\partial_\xi F + \frac{1}{6}\hat{\eta}\widehat{Ra_2}y^3\partial_\xi F - \partial_y\psi_2\partial_\xi F + 40\hat{\eta}y\partial_\xi F$$

$$- 100\hat{\eta}y^2\partial_\xi T_2 + \frac{160}{3}\hat{\eta}y^3\partial_\xi T_2 - \partial_y\psi_0\partial_\xi F + \partial_\xi^2 T_2 = 0. \tag{6.10}$$

To obtain the governing evolution equation for $F(\xi, \tau)$, the solution at $O(\epsilon^2)$ given by (6.9) needs to be substituted into (6.10), and the latter is integrated with respect to y across the layer $y \in (0, 1)$ along with the appropriate boundary conditions. As a result, we obtain the governing evolution equation for $F(\xi, \tau)$ in the form

$$\partial_\tau F + \frac{58}{693}\partial_\xi^4 F - \left[\frac{1}{6}\hat{\eta} + \frac{5\hat{\eta}}{42Pr}\right]\partial_\xi^3 F + \frac{1}{12}\partial_\xi^2\left[(\partial_\xi F)^2\right]$$
$$+ \left[-\frac{760}{189}\hat{\eta}^2 + \frac{1}{320}\widehat{Ra_2} + \frac{1520}{189}\hat{\eta}\partial_\xi F - \frac{760}{189}(\partial_\xi F)^2\right]\partial_\xi^2 F + \widehat{Bi}\, F = 0, \qquad (6.11)$$

where the Biot number term $\widehat{Bi}F$ arises due to the heat transfer boundary condition at the free surface $y = 1$ at $O(\epsilon^4)$. Before proceeding further we scale out ϵ from the above equation by using the scaling (6.4a–e) expressing the system dynamics in terms of the unscaled dimensionless variables and parameters to obtain

$$\partial_t F + \frac{58}{693}\partial_x^4 F - \eta\left[\frac{1}{6} + \frac{5}{42Pr}\right]\partial_x^3 F$$
$$+ \partial_x\left[\left(\frac{1}{320}Ra_2 - \frac{760}{189}\eta^2 + \frac{760}{189}\eta\partial_x F - \frac{760}{567}(\partial_x F)^2 + \frac{1}{6}\partial_x^2 F\right)\partial_x F\right] + BiF = 0, \qquad (6.12)$$

where $Ra_2 = \epsilon^2\widehat{Ra_2}$. The analyses below are carried out based on the evolution equation (6.12).

6.2. *Linear stability analysis*

To carry out the linear stability analysis of the base state corresponding to $F = 0$, we substitute $F(x, t) = \zeta \exp(i(kx - \omega t))$ into (6.12) where $\zeta \ll 1$ is an arbitrary constant. Upon linearization and further simplification, we obtain the dispersion relation

$$\omega = \frac{\eta k^3(5 + 7Pr)}{42Pr} + i\left[-Bi + Rk^2 - \frac{58k^4}{693}\right], \qquad (6.13)$$

where

$$R = \frac{Ra_2}{320} - \frac{760\eta^2}{189}. \qquad (6.14)$$

The real and imaginary parts of (6.13) are

$$\omega_r = \frac{\eta k^3(5 + 7Pr)}{42Pr}, \qquad (6.15a)$$

$$\omega_i = -Bi + Rk^2 - \frac{58k^4}{693}. \qquad (6.15b)$$

The variation of the growth rate ω_i, i.e. the imaginary part of ω, as a function of the wavenumber k with an increase in η is presented in figure 10. In agreement with the GLSA, an increase in the HTG η has a strong stabilizing effect on the long-wave mode introduced by the VTG.

Since at $k = 0$ the growth rate $\omega_i = -Bi$ is negative and in the limit of $k \to \infty$ the growth rate $\omega_i \sim -k^4$ is also negative, the stability properties of the system are determined
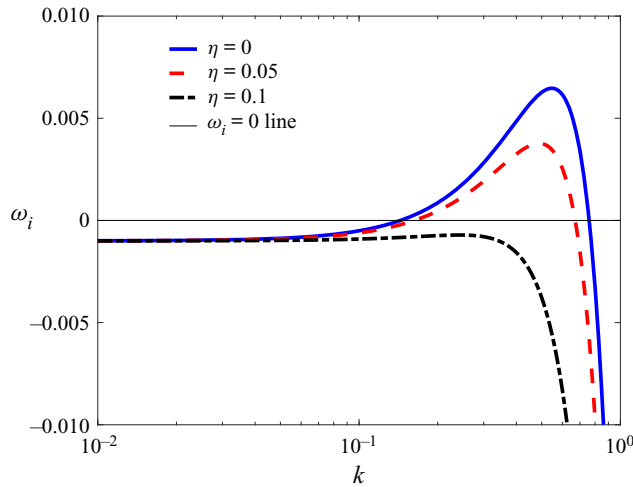
Figure 10. Variation of the growth rate ω_i with the wavenumber k at $Bi = 0.001$, $Pr = 10$ and $Ra_2 = 16$ for various η as given by (6.15b). The figure illustrates a strong stabilizing effect of the increase in the relative strength of the HTG η on the long-wave mode induced by the imposed VTG.

via the sign of the maximal value of ω_i in the intermediate range. This leads to the result that along the neutral stability curve, i.e. $\omega_i = 0$,

$$Ra_2 = \frac{243\,200}{189}\eta^2 + 640\sqrt{\frac{58}{693}Bi}. \tag{6.16}$$

The critical Rayleigh number up to $O(\epsilon^2)$ correction is thus

$$Ra_c = Ra_0 + Ra_2 = 320 + \frac{243\,200}{189}\eta^2 + 640\sqrt{\frac{58}{693}Bi}. \tag{6.17}$$

This clearly illustrates the stabilizing effect of an increase in η via an increase in the critical Rayleigh number Ra_c on the long-wave mode in agreement with the GLSA.

Similarly, the effect of an increase in the Biot number Bi is also stabilizing, as seen in figure 11, which presents the variation of the growth rate ω_i with the wavenumber k and the Biot number Bi for $\eta = 0$ and $Ra_2 = 16$ representing 5 % supercriticality. Due to the presence of heat transfer at the free surface, $Bi \neq 0$, the long-wave mode $k \to 0$ is linearly stable. Similarly, short waves are damped due to dissipation promoted by viscosity and thermal diffusivity of the liquid, $\omega_i < 0$ for $k \gg 1$. This leaves an intermediate (still long-wave) range of the disturbance wavenumber k to exhibit instability $\omega_i > 0$, and gives rise to the emergence of two values of k, $k = k_1 \approx 0.133$ and $k = k_2 \approx 0.774$ for $Bi = 0.001$, where the growth rate ω_i vanishes. The fastest growing linear mode $k = k_m$ is determined as usual via solution of the equation $\mathrm{d}\omega_i/\mathrm{d}k = 0$, which yields in the case of $Bi = 0.001$, $k = k_m \approx 0.5465$. We refer to this figure below in discussion of the results in the context of nonlinear dynamics of the system revealed via numerical solution of the evolution equation (6.12).

Figure 12 displays a comparison of Ra_c obtained from both the numerical and long-wave analyses. An excellent agreement between the two approaches for $\eta < 0.2$ proves the validity of the long-wave asymptotic analysis. It is noteworthy that, as follows from (6.17), the maximal value of the second-order correction is ≈ 31.5 for $\eta < 0.1$ and $Bi \leq 0.01$, which is much smaller (about 10 %) than $Ra_0 = 320$.
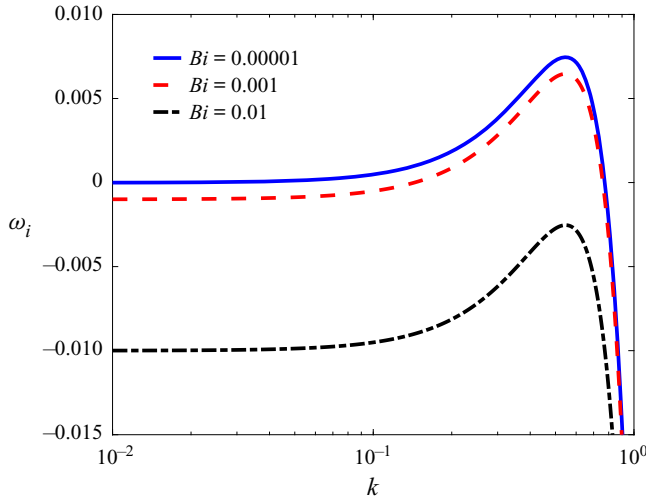
Figure 11. Growth rate ω_i as a function of the wavenumber k for $Ra_2 = 16$ and $\eta = 0$ as given by (6.15b) for different Bi. Note that the growth rate ω_i is independent of the Prandtl number Pr.
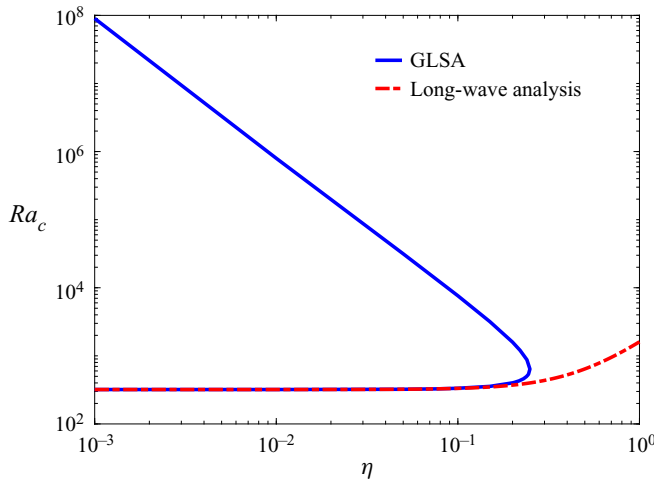

Figure 12. Variation of Ra_c with η at $Pr = 10$ and $Bi = 10^{-5}$. Along the lower branch, the analytically obtained value of Ra_c given by (6.17) is in excellent agreement with the values of Ra_c determined numerically for $\eta < 0.2$, thereby validating the former.

6.3. *Spatio-temporal linear stability analysis*

In this subsection, for the sake of simplicity, we present the results for the case of $Bi = 0$, which remain practically unaffected for small but non-zero Bi ($< O(10^{-4})$). To carry out the temporal stability analysis, ω is taken as a complex number, while the wavenumber k is treated as a real number (Drazin & Reid 1981). To investigate the spatial stability analysis aimed at determining the evolution of disturbances in space, the frequency ω is treated as a real number while k is a complex number (Drazin 2002). Conversely, in a spatio-temporal stability analysis, both ω and k are treated as complex numbers (Huerre & Monkewitz 1990; Schmid & Henningson 2001). This section is aimed at understanding the impact of the HTG on the emergence of absolute instability.

An instability is classified as either absolute or convective if the growth of disturbances takes place in both upstream and downstream directions or the disturbances develop in the downstream direction from their source, respectively (Briggs 1964; Huerre & Monkewitz 1990; Schmid & Henningson 2001). The proposed methodology to determine the existence of absolute instability is by progressively moving the Laplacian contour in the ω_r–ω_i plane and the Fourier contour in the k_r–k_i plane (Briggs 1964).

Thus, in the case of convective instability, the disturbances will decay at any fixed position in space if sufficient time is allowed for that (Huerre & Monkewitz 1990). This results in mixing in the downstream direction only, whereas absolute instability will induce mixing in both upstream and downstream directions. The emergence of absolute or convective instability can be illustrated by considering the response of a given base velocity profile to an impulse excitation at asymptotically long times (Huerre & Monkewitz 1990).

The emergence of absolute instability for a given dispersion relation $\omega = g(k)$ with a continuous and differentiable function $g(k)$ can be detected if the group velocity of the disturbances has at least one saddle point, i.e. there exists at least one root k for the equation $\partial \omega / \partial k = 0$ (Huerre & Monkewitz 1990; Schmid & Henningson 2001). However, the determined saddle point must also obey the causality principle for the existence of absolute instability (Huerre & Monkewitz 1990).

To obtain a sufficient condition for the emergence of absolute instability, the equation $\partial \omega / \partial k = 0$ is solved in terms of k, which yields the saddle points of the dispersion relation. If the saddle point $k = k_0$ is of first order in the k plane, then a local Taylor expansion for ω about this point yields $(\omega - \omega_0) \sim (k - k_0)^2$, where $\omega_0 \equiv \omega(k_0)$. This shows that the mapping from the k plane ($k = k_r + \mathrm{i}k_i$) to the ω plane ($\omega = \omega_r + \mathrm{i}\omega_i$) for a first-order saddle point is characterized by angle doubling. Note that the k and ω planes are spanned over k_r–k_i and ω_r–ω_i, respectively.

For realistic dispersion relations, finding a saddle point in the k plane and a cusp point in the ω plane according to the method of Briggs (1964) becomes a cumbersome mathematical and numerical task. A simpler alternative is the method of Kupfer, Bers & Ram (1987), in which for a prediction of absolute instability, only the formation of a cusp point in the ω plane is necessary. Figure 13 illustrates a genuine cusp point in the ω plane, thereby illustrating the existence of absolute instability for a non-zero η.

For $\eta = 0$, (6.13) yields $\omega_r = 0$; thus disturbances do not travel and $\omega_i > 0$ for $Ra_2 > 0$ for a range of sufficiently low k. Thus, in the absence of the imposed HTG, the flow is absolutely unstable and the critical Rayleigh numbers for the onset of the temporal and absolute instabilities are equal. However, for $\eta > 0$, $\omega_r \neq 0$, and the flow may become convectively unstable as illustrated in figure 14.

Given a simple structure of the dispersion relation (6.13), the location of a saddle point in the k plane and that of a cusp point in the ω plane is readily obtained. Differentiating (6.13) with respect to k once and then solving the equation $\mathrm{d}\omega / \mathrm{d}k = 0$ yields a saddle point:

$$
k_0 = -\mathrm{i} \frac{1485\eta(5 + 7\,Pr)}{13\,920\,Pr}
$$
$$
+ \frac{\sqrt{3\,617\,460\,Pr^2\,Ra_2 - 825\eta^2\,[66\,825 + Pr(187\,110 + 5\,773\,217Pr)]}}{13\,920\,Pr}. \tag{6.18}
$$

A mirror saddle point with $k_r < 0$ and the same k_i also exists as the second solution of the equation $\partial \omega / \partial k = 0$. Since we consider now a solution with $k_r > 0$ only, the saddle
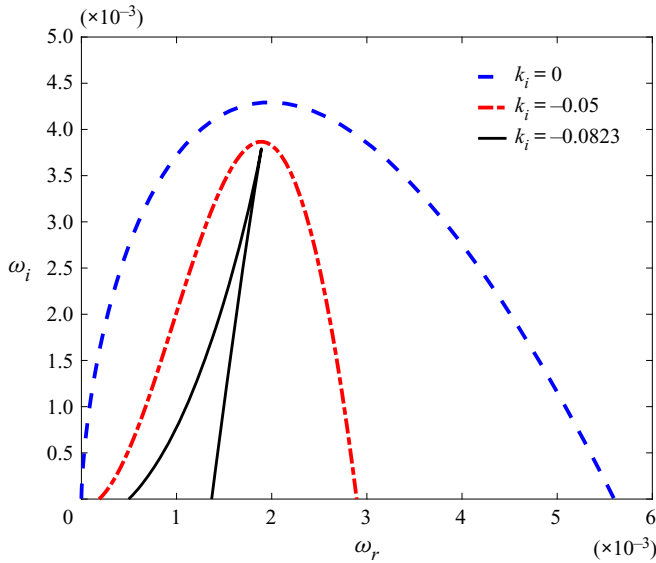
Figure 13. Cusp point formation at $Pr = 7$, $Ra_2 = 25$, $\eta = 0.1$ and $Bi = 0$. The figure illustrates the existence of absolute instability for a non-zero η in the ω_r–ω_i plane. The cusp point is located at $\omega_0 = 0.00189 + 0.00379i$. A straight curve drawn from the cusp point $\omega = \omega_0$ intersects the $k_i = 0$ curve once, i.e. an odd number of times, thereby confirming the genuine nature of the cusp point. The cusp point corresponds to $\omega_{i0} > 0$; thus for the chosen parameter set, the system is absolutely unstable.
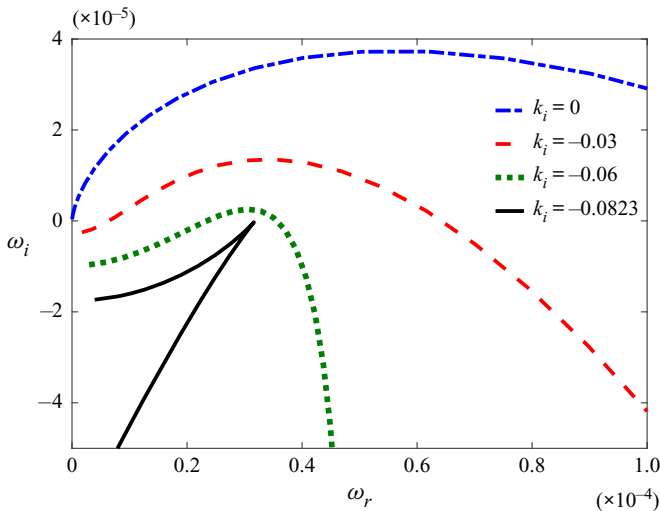

Figure 14. Cusp point formation in the case of $Pr = 7$, $Ra_2 = 14$, $\eta = 0.1$ and $Bi = 0$. The cusp point is located at $\omega_0 = 3.1626 \times 10^{-5} - 2.9339 \times 10^{-7}i$, and corresponds to $\omega_{i0} < 0$; thus the system with a given parameter set is convectively unstable.

point with $k_r < 0$ will not be used henceforth. It must be noted that the saddle point with $k_r < 0$ corresponds to the cusp point with $\omega_r < 0$ and both saddle points will yield the same value of ω_{i0}. We now substitute $k = k_0$ into (6.13) and obtain the corresponding value $\omega_0 = \omega(k_0)$. The variation of the critical parameters for the emergence of the temporal and
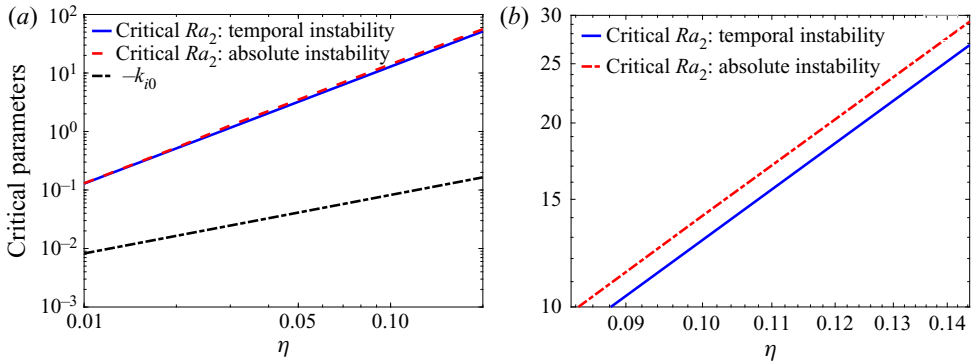
Figure 15. Variation of the critical parameters at $Pr = 7$ and $Bi = 0$. (*a*) The difference between the critical Ra_2 for the thresholds of the temporal and absolute instabilities and k_{i0} increases with an increase in η, thereby showing the role of the imposed HTG in the emergence of convective instability. (*b*) A magnified part of (*a*) to emphasize the existence of the convectively unstable streamwise mode.
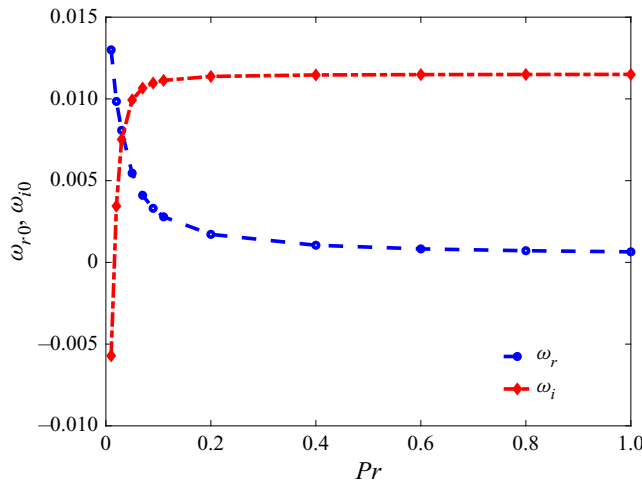

Figure 16. Variation of the cusp point location ($\omega_0 = \omega_{r0} + i\omega_{i0}$) with Pr at $Ra_2 = 20$, $\eta = 0.01$ and $Bi = 0$.

absolute instabilities and the value of k_{i0} is shown in figure 15. For example, for $\eta = 0.1$, the critical values for Ra_2 in the cases of the temporal and absolute instabilities are $\sim$12.88 and $\sim$14.1, respectively. Also, with $\eta = 0$, the critical values Ra_2 for the emergence of the temporal and absolute instabilities are equal to zero.

Variation of the cusp point location in the ω plane with the Prandtl number Pr is presented in figure 16. It follows from the governing equations (2.2*b*) that with a decrease in Pr, the inertial terms become more important. This leads to a stronger convection, thereby even resulting in the convective instability at sufficiently low Pr. On the other hand, as Pr increases, the flow becomes absolutely unstable with a rapid initial rise in the growth rate ω_i until $Pr \sim 0.2$ where the latter achieves a constant value which remains the same with a further increase in Pr.

937 A11-26

6.4. *Weakly nonlinear analysis*

Similar to the previous subsection, for the sake of simplicity, we present the results in the case of $Bi = 0$ which remain practically unaffected for small but non-zero Bi ($< O(10^{-4})$). To carry out the weakly nonlinear stability analysis, we follow the approach used by Cheng, Chen & Lai (2001), Oron & Bankoff (1999) and Patne *et al.* (2021*a*) and introduce slow time scales $T_1 = \delta t$, $T_2 = \delta^2 t$, where $\delta \ll 1$ is a small parameter related to the deviation of the Rayleigh number Ra from its critical value Ra_c via (6.19*a*). The Rayleigh number Ra and the temperature disturbance $F(x, t)$ are expanded into series of δ as

$$Ra_2 = Ra_{2c}(1 + \delta^2), \tag{6.19a}$$

$$F(x, t) = 1 + \delta F_1(x, t, T_1, T_2) + \delta^2 F_2(x, t, T_1, T_2) + \delta^3 F_3(x, t, T_1, T_2) + \cdots, \tag{6.19b}$$

where Ra_{2c} is the critical value of the Rayleigh number obtained by solving (6.15*b*) for $\omega_i = 0$ with $k = k_c = 2\pi/L$ being the cut-off wavenumber and L the length of the periodic domain, namely

$$-Bi + \left(\frac{Ra_{2c}}{320} - \frac{760\eta^2}{189} \right) k_c^2 - \frac{58}{693} k_c^4 = 0. \tag{6.20}$$

These are substituted into (6.12). The problem is then solved order by order in δ in terms of F_i.

At first order in δ, the correction to the temperature disturbance F_1 due to the perturbations is obtained in the form

$$F_1(x, t, T_1, T_2) = a(T_1, T_2) \exp\left(i(k_c x - \omega_r t)\right) + \text{c.c.}, \tag{6.21}$$

where $a(T_1, T_2)$ is the complex amplitude of the perturbation, yet unknown, evolving in slow time and c.c. denotes complex conjugate. At second order in δ, the solvability condition yields that the complex amplitude A is independent of the slow time scale T_1, namely $A = A(T_2)$. Also, the solution of the differential equation at second order is exponential similar to F_1 above, namely $F_2(x, t, T_1, T_2) = b(T_2) \exp[(2i(k_c x - \omega_r t)] + $ c.c. with the complex amplitude $b(T_2)$ proportional to $a(T_2)^2$.

Finally, at third order in δ, the Landau equation governing the temporal evolution of the amplitude function $a \equiv a(T_2)$ in slow time T_2 is obtained:

$$\partial_{T_2} a = \lambda_1 a + \lambda_2 |a|^2 a, \tag{6.22a}$$

where λ_1 and λ_2 are the Landau parameters:

$$\lambda_1 = \delta^{-2} k_c^2 (Ra_2 - Ra_{2c}), \quad \lambda_2 = \frac{\lambda_{2n}}{\lambda_{2d}} - \frac{760}{189} k_c^4, \tag{6.22b}$$

where

$$\lambda_{2n} = 880(1520\eta + 63ik_c)(3040\eta + 63ik_c)k_c^6 Pr, \tag{6.22c}$$

$$\lambda_{2d} = 189[320k_c^2(8360\eta^2 Pr + 696k_c^2 Pr + 99i\eta k_c(5 + 7Pr))$$
$$- 2079k_c^2 Pr Ra_{2c} - 332\,640i Pr \omega], \tag{6.22d}$$

and $\omega = \omega_r + i\omega_i$. Recall that at the stability threshold, the complex frequency is real, i.e. $\omega = \omega_r$. As usual, the linear term on the right-hand side of the Landau equation (6.22*a*) is associated with the value of supercriticality Ra_2–Ra_{2c} and that the cubic coefficient of the Landau equation λ_2 is in general complex due to wave propagation.
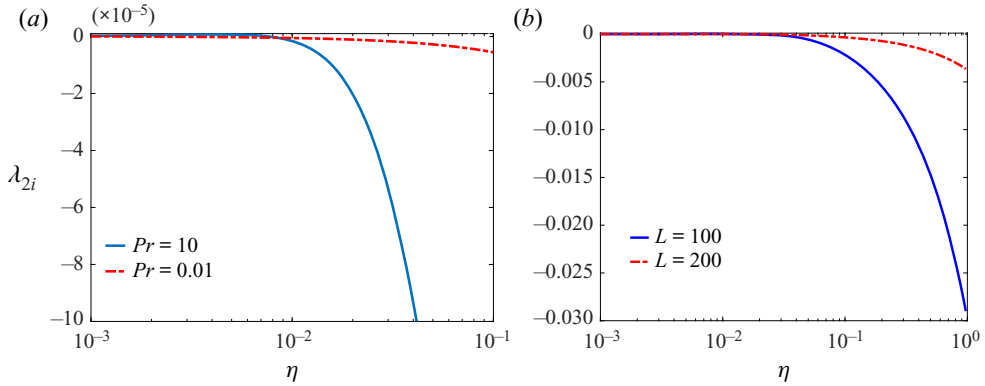
Figure 17. Variation of the imaginary part of the Landau coefficient λ_{2i} with η at select values of (*a*) *Pr* and (*b*) *L*. A non-zero λ_{2i} for $\eta \neq 0$ indicates the change in the bifurcation from pitchfork with $\eta = 0$ to Hopf bifurcation.

For a liquid layer subjected to a purely VTG, namely $\eta = 0$, the Landau equation (6.22*a*) is real, since then $\omega = 0$ at the stability threshold, and thus λ_2 is real and negative. Therefore, the system undergoes a pitchfork (supercritical) bifurcation. In the case of a liquid layer subjected to a purely VTG when both bounding surfaces are rigid (Gertsberg & Sivashinsky 1981), the bifurcation is also supercritical provided that the fluid viscosity is constant.

In the case of $\eta \neq 0$, the Landau equation (6.22*a*) is complex. For sufficiently low values of η, the real part of λ_2 remains negative, $\lambda_{2r} < 0$. Thus, the imposed HTG does not affect the supercritical type of bifurcation; however, for non-zero HTG, $\eta \neq 0$, owing to the presence of the imaginary part of λ_2, the bifurcation changes from pitchfork to Hopf bifurcation, as shown in figure 17.

6.5. *Nonlinear dynamics of the system*

This subsection is devoted to the numerical investigation of the evolution equation (6.12) formulated in terms of the function F representing the leading-order perturbation of the temperature field with respect to the base-state distribution of the temperature in the layer.

Equation (6.12) is numerically solved with periodic boundary conditions in the domain $0 \leq x \leq L$ and the initial condition

$$F(x, t = 0) \equiv F_0 = \delta \cos\left(\frac{2\pi x}{L}\right), \tag{6.23}$$

where δ is a small number, typically $\delta = 0.1$. We use the numerical technique based on the Newton–Kantorovich method presented in Boyd (2001) and implemented for solution of a single partial differential equation (Oron 2000; Oron & Gottlieb 2002). We refer the reader to details presented there. Typical values of the number of grid points in the periodic domain and the time step sufficient for convergence are 400–1000 varying with the parameter set of (6.12) and $O(10^{-3})$, respectively.

In the case of $\eta = 0$, the system is subjected to a purely VTG and preserves left–right symmetry. Figure 18 presents a typical outcome of the spatio-temporal evolution of the temperature disturbance F for $\eta = 0$, $Bi = 0$ and $Ra_2 = 16$ with the spatial periodicity of $L = L_m$, $L = 2L_m$, $L = 4L_m$ and $L = 8L_m$, as displayed by curves 1–4, respectively. Note that in the case of $\eta = 0$, the Prandtl number does not affect the evolution of the
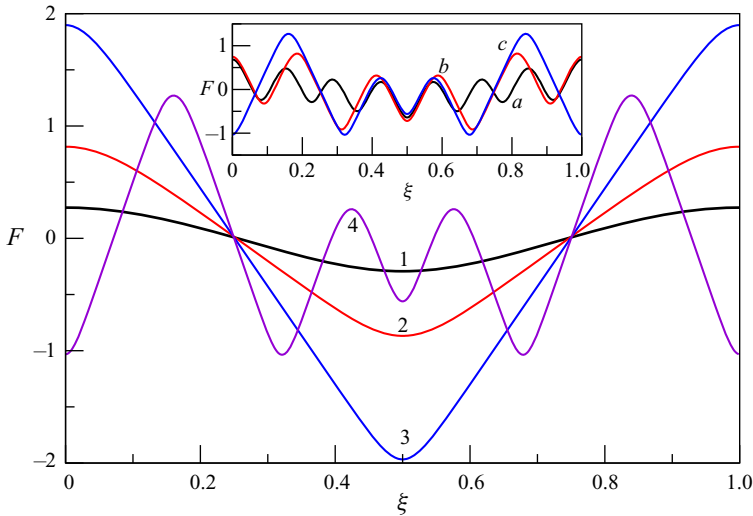
Figure 18. Evolution of the temperature disturbance F in the framework of (6.12) with $\eta = 0$, $Bi = 0$ and $Ra_2 = 16$. Here $\xi = x/L$. Curves 1, 2 and 3 correspond to the steady states of the system with $L = L_m$ and $L = 2L_m$ both at $t = 4000$, and with $L = 4L_m$ at $t = 20\,000$. Curve 4 corresponds to the transient of the system with $L = 8L_m$ at $t = 100\,000$. The inset illustrates a coarsening process in the system with $L = 8L_m$ at $t = 5000$, $t = 10\,000$ and $t = 100\,000$ shown by curves a, b and c, respectively. Curve c in the inset and curve 4 in the main figure are the same.

temperature field and therefore does not appear in the parameter list. We also note that a formal use of $Bi = 0$ represents well the results obtained for $Bi \lesssim 10^{-5}$. The value of L_m represents the wavelength of the fastest-growing linear mode, $L_m = 2\pi/k_m$. The layer evolution is slow and is characterized by the tendency of coarsening, so at the end, one cell of the maximal horizontal extent will emerge. Curves 1, 2 and 3 show steady states of F at $t = 4000$, $t = 4000$ and $t = 20\,000$, respectively. For the sake of convenience of presentation the horizontal spatial variable is scaled with respect to the periodicity L, $\xi = x/L$. Curve 4 displays a transient state of F at a very large time $t = 100\,000$. The coarsening dynamics is displayed in the inset, which shows its main stages at $t = 5000$, $t = 10\,000$ and $t = 100\,000$ marked by a, b and c, respectively. The temperature distribution at these times exhibits 7, 5 and 4 humps, respectively. We conjecture that at even larger times, the humps seen in curve 4 will merge and their number will further decrease, so at the end of the evolution, a one-hump pattern taking the entire periodic domain, similar to curves 1–3 in the figure itself, will form. This type of dynamics could be expected since a hot liquid parcel rising to the layer free surface will travel the longest possible distance along it before sinking by retaining heat and not releasing it to ambient since $Bi = 0$ (or releasing it extremely slowly for $Bi \leq 10^{-5}$). On the other hand, with a larger Bi, e.g. $Bi = 0.001$, the heat loss to ambient takes place faster; therefore, a liquid parcel moving along the film interface is expected to travel a finite distance before its temperature decreases and it sinks. As a result of this, a number of convective cells is expected to emerge for these values of Bi, and we turn to this case next.

Figure 19 presents the results of a typical evolution of the temperature disturbance F in the case of a moderately small non-zero Biot number, e.g. $Bi = 0.001$, with $\eta = 0$ and $Ra_2 = 16$. Figure 19(a) depicts the time evolution of the maximal F_{max} and minimal F_{min} values of F for the cases of $L = L_m$, $L = 2L_m$, $L = 4L_m$ and $L = 8L_m$ marked by 1–4, respectively. While in the cases of $L = L_m$ and $L = 2L_m$, the longest mode $\exp{(2i\pi x/L)}$
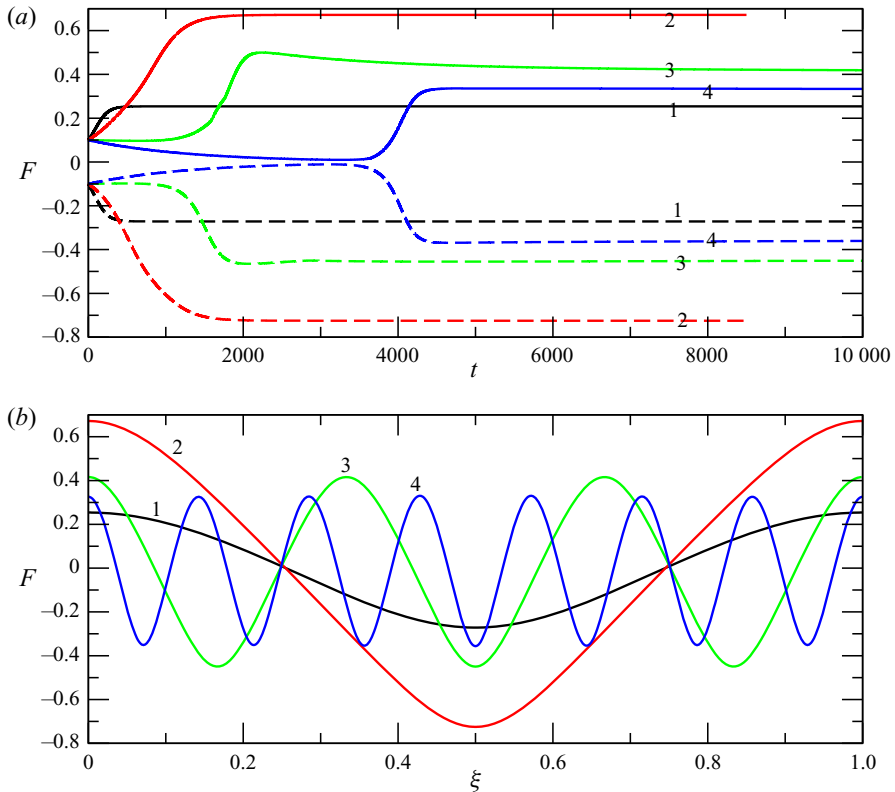
Figure 19. Evolution of the temperature disturbance F in the framework of (6.12) with $\eta = 0$, $Bi = 0.001$ and $Ra_2 = 16$. Note that in the case of $\eta = 0$, the Prandtl number does not affect the dynamics of the system. Here $\xi = x/L$. (*a*) Temporal evolution of the maximal and minimal values of F shown by solid and dashed curves, respectively. Curves 1–4 correspond to the system with $L = L_m$, $L = 2L_m$, $L = 4L_m$ and $L = 8L_m$, respectively. (*b*) Profiles of F. Curves 1–4 show steady states of the system with $L = L_m$ at $t = 5000$, $L = 2L_m$ at $t = 6000$, $L = 4L_m$ at $t = 25\,000$ and $L = 8L_m$ at $t = 25\,000$, respectively.

admissible in the domain of size L is linearly unstable for the given set of parameters, and thus F_{max} increases and F_{min} decreases in the short-time range, the two other cases evolve differently. As shown in figure 11, due to the fact that the range of small wavenumbers k belongs to the linearly unstable range, for a sufficiently long periodic domain, in 'short' times, the initial disturbance of F decays. This takes place for the cases shown by curves 3 and 4 in figure 19(*a*). Following this decay, the nonlinearities present in (6.12) transfer a sufficient amount of energy into higher modes, so the energetically dominant mode enters the linearly unstable domain, and the temperature disturbance grows in time and then saturates. In the long-time limit, the amplitude of F tends to constants for both F_{max} and F_{min}.

Figure 19(*b*) displays steady states for all the four cases reached each at its time. In these cases with $L = NL_m$, $N = 1, 2, 4$ and 8 shown here, the fastest-growing linear modes $k = 2j\pi/L$ correspond to $j = N$. Since the steady states presented in figure 19(*b*) display one convective cell for the cases of $L = L_m$ and $L = 2L_m$, and three and seven cells in the cases of $L = 4L_m$ and $L = 8L_m$, respectively, the following conclusion is drawn: the wavelength of the steady pattern is larger than that of the fastest-growing linear mode, except for the basic case of $L = L_m$.
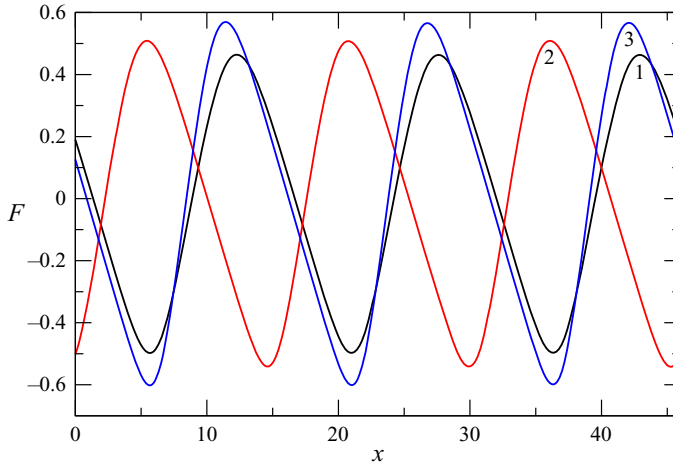
937 A11-30

Figure 20. Evolution of the temperature disturbance F in the framework of (6.12) with $Bi = 0.001$ and $Pr = 6.7$ for various values of η with supercriticality of 5 %, namely $Ra_2 = 1.05Ra_c - 320$ and $L = 4L_m$. Curves 1–3 correspond to the travelling waves at $t = 25\,000$ with the parameter sets of ($\eta = 0.05$, $Ra_2 = 19.2169$), ($\eta = 0.075$, $Ra_2 = 23.2381$) and ($\eta = 0.1$, $Ra_2 = 28.8677$), respectively.

A typical example of the long-time evolution of the temperature field is shown in figure 20, which presents stationary wave states of the system at $t = 25\,000$ for three parameter sets with $\eta = 0.05$, 0.075 and 0.1 with supercriticality of 5 %, namely $Ra_2 = 1.05Ra_c - 320$ for each of the cases. The values of the Biot and Prandtl numbers are fixed at $Bi = 0.001$ and $Pr = 6.7$, and the size of the periodic domain is $L = 4L_m$. As in the case of $\eta = 0$ shown in figure 19, the patterns display three humps, but this time, they travel to the right, i.e. against the direction of the HTG, as travelling waves (the corresponding phase plane portraits are closed curves – not shown) with a speed of $c = 0.0004$, 0.0006 and 0.0008 evaluated numerically in cases 1–3, respectively. The propagation direction of these travelling waves of the temperature disturbances is in accord with the result of the linear stability theory given by (6.15a). As a reference, in the case of the parameter sets corresponding to the curves displayed in figure 20, the corresponding wave speeds as predicted by the linear stability analysis are $c_{lin} = \omega_r/k = 0.0015$, 0.0023 and 0.0031 for $\eta = 0.05$, 0.075 and 0.1, respectively, where k is the actual wavenumber of the travelling wave; in our case in figure 20, $k = L/3$. It is interesting to note that the values of the travelling wave speed c are lower than those for c_{lin} and are roughly proportional to η, as predicted in the linear stability theory for ω_r by (6.15a) along with $c_{lin} = \omega_r/k$.

Knobloch (1990) investigated various versions of the weakly nonlinear evolution equations emerging in long-wave convection. However, since the equation investigated there possesses an even parity with respect to the independent variables, the results obtained there cannot be applied in our case, where (6.12) contains among the same terms as in Knobloch (1990) two additional terms, namely the dispersive term proportional to $\partial_x^3 F$ and the term proportional to $\partial_x[(\partial_x F)^2]$, which have a broken parity. Both of these terms emerge from the presence of the imposed HTG.

As mentioned above, the presence of the dispersive term $\sim F_{xxx}$ begets thermal wave propagation against the direction of the imposed HTG. It turns out that the presence of the other broken-parity term $\partial_x[(\partial_x F)^2]$ induces a special property of the wave shape.

937 A11-31

Frequently, evolution equations with a broken left–right symmetry, which describe instabilities in a liquid layer, contain the advection term of the form FF_x like in the nonlinear wave equation. In these cases, the sign of the coefficient of the advection term designates the direction of the wave propagation. If it is positive (negative), the wave travels to the right (left). Accordingly, the leading front of the wave is steeper than its rear front. In the case at hand, (6.12) does not feature this term; instead of it, $\partial_x^3 F$ and $\partial_x(\partial_x F)^2$ are present.

In the case of $\eta \neq 0$, the waves displayed in figure 20 travel to the right according to the sign of the dispersive term $\sim \partial_x^3 F$ and (6.15a) and show asymmetric shapes where the rear fronts are steeper than their leading fronts. Let us now explain this effect imparted by the term $\partial_x[(\partial_x F)^2]$. To do this consider the equation

$$\partial_t F + \frac{760}{189}\eta\partial_x[(\partial_x F)^2] = 0. \tag{6.24}$$

Differentiating (6.24) with respect to x and defining $\phi = F_x$ yields the equation

$$\partial_t \phi + \frac{1520}{189}\eta\partial_x\left(\phi\partial_x\phi\right) = 0, \tag{6.25}$$

which displays backward diffusion of ϕ (instability) for $\phi > 0$ and forward diffusion of ϕ for $\phi < 0$, namely for the increasing and decreasing branch of the function $F(x,t)$, respectively. This causes a stretching with time, i.e. an increase in the variation of ϕ equivalent to an increase in the gradient of F with time along the increasing branch of F. The opposite takes place along the decreasing branch of F, where the variation of ϕ tends to decrease with time, as usual for a normal (forward) diffusion, which materializes in a decrease in the gradient $\partial_x F$. These changes ensuing from the presence of the term proportional to $\partial_x[(\partial_x F)^2]$ increase proportionally to the value of η and can be seen in figure 20, where the increasing branches (rear fronts) are always steeper than the decreasing ones (leading fronts). We reiterate that this feature is opposite to that of well-known travelling waves driven by advection FF_x as in the nonlinear wave equation where the leading front will be always steeper than the rear one.

We note that (6.12) is not invariant under the following mappings: $F \to -F$, $(F \to -F,\ x \to -x)$ and $(F \to -F,\ x \to -x, \eta \to -\eta)$. As a result, the temperature distributions F are asymmetric with respect to the line $F = 0$, namely $|F_{max}| \neq |F_{min}|$. It is observed that the spatial variation of the temperature disturbance indeed satisfies this observation, and in all solutions presented here in figures 18–20 except for curve 4 in figure 18 which still evolves in time and space, $|F_{max}| < |F_{min}|$. Also, it is found that both the temperature amplitude F_{max} and peak-to-peak size of the temperature wave $F_{max} - F_{min}$ grow with η, as illustrated in figure 20.

We next explore the nonlinear evolution of a layer for a varying Prandtl number Pr. To do this, we chose a silicone oil with Prandtl number of $Pr = 50$. The Prandtl number appears in the dispersive term $\sim F_{xxx}$, and, as suggested by the linear stability analysis based on (6.12), affects its critical wave speed ω_r; see (6.15a). The critical speed ω_r decreases with an increase of Pr. We have found numerically that the speed of a travelling wave pattern indeed decreases with Pr. It is interesting to note that in flow regimes with $Pr = 50$, the values of F_{max} and F_{min} are equal to their respective values in the regimes displayed in figure 20 for $Pr = 6.7$. We thus conjecture that the Prandtl number does not affect the maximal and minimal values of the amplitude of the temperature variation in the saturated travelling wave regime with the rest of the parameters fixed.

7. Conclusions

The present work deals with the buoyancy instability in a liquid layer subjected to an OTG resting on a poorly conducting horizontal substrate and bounded by a free non-deformable interface separating the liquid and the ambient gas phase. The GLSA reveals a strong stabilizing effect of the imposed HTG on the buoyancy instability triggered by the imposed VTG for $Pr > 1$. The imposed HTG stabilizes the instability caused by the imposed VTG by inducing a VTG which opposes the imposed VTG. For $Pr < 1$, relevant to liquid metals, a new mode of instability arises as a result of the velocity jump in the liquid layer and the presence of inertia.

Exploiting the long-wave nature of the instability introduced by the VTG in the case of low Biot numbers, we carry out a long-wave nonlinear analysis and derive the evolution equation governing the weakly nonlinear spatio-temporal dynamics of the leading-order perturbations to the base-state temperature field. The linear stability analysis based on this evolution equation confirms the stabilizing effect of the imposed HTG. The spatio-temporal stability analysis predicts the existence of convective instability due to the imposed HTG. The critical parameters for the onset of the temporal and absolute instabilities are equal in the absence of an imposed HTG. However, in the presence of the HTG, the critical parameters for the onset of the absolute instability are higher than those for the temporal instability and the emergence of convective instability is possible. The weakly nonlinear analysis based on the aforementioned evolution equation reveals the change of the bifurcation from pitchfork to Hopf for a non-zero HTG.

Numerical investigation of the weakly nonlinear dynamics of the temperature disturbances' field based on the evolution equation derived here shows that instead of time-independent flow emerging in the absence of an imposed HTG, the latter leads to the formation of travelling cells propagating against the direction of the imposed HTG with a speed roughly proportional to the strength of the HTG. The wavelength of the stationary travelling temperature disturbance pattern emerging in the nonlinear stage of the evolution is found to be larger than the wavelength of the fastest-growing linear mode.

A comparison between the stability properties of the buoyancy instability with the companion physical setting of the thermocapillary instability considered elsewhere by Patne *et al.* (2021*a*) both driven by an OTG reveals a possibility of the emergence of the thermocapillary instability in a thick liquid layer in the case of Prandtl number larger than one. This paper calls for an experimental verification of this phenomenon.

In the present paper, we have considered the case of a horizontal layer of a Newtonian liquid. However, many practical applications and industrial processes involve non-isothermal horizontal layers of non-Newtonian fluids subjected to an either intentionally or unintentionally created OTG. Also, to ease on technicalities we have assumed a temperature-independent viscosity of the fluid, whose possible variation with temperature may lead to a modification in the critical parameters obtained here. The present investigation is to be extended to include this effect along with the non-Newtonian nature of the fluid.

Declaration of interests. The authors report no conflict of interest.

Author ORCIDs.
- Ramkarn Patne https://orcid.org/0000-0003-4052-1807;
- Alexander Oron https://orcid.org/0000-0002-0383-388X.

REFERENCES

BOYD, J.P. 2001 *Chebyshev and Fourier Spectral Methods*, 2nd edn. Dover.

BRAUNSFURTH, M.G., SKELDON, A.C., JUEL, A., MULLIN, T. & RILEY, D.S. 1997 Free convection in liquid gallium. *J. Fluid Mech.* **342**, 295–314.

BRIGGS, R.J. 1964 *Electron-Stream Interaction with Plasmas*. MIT Press.

CHAPMAN, C.J. & PROCTOR, M.R.E. 1980 Nonlinear Rayleigh–Bénard convection between poorly conducting boundaries. *J. Fluid Mech.* **101** (4), 759–782.

CHENG, P.J., CHEN, C.K. & LAI, H.Y. 2001 Nonlinear stability analysis of thin viscoelastic film flow traveling down along a vertical cylinder. *Nonlinear Dyn.* **24**, 305–332.

DRAZIN, P.G. 2002 *Introduction to Hydrodynamic Stability*. Cambridge University Press.

DRAZIN, P.G. & REID, W.H. 1981 *Hydrodynamic Stability*. Cambridge University Press.

GERTSBERG, V.L. & SIVASHINSKY, G.I. 1981 Large cells in nonlinear Rayleigh–Bénard convection. *Prog. Theor. Phys.* **66**, 1219.

GILL, A.E. 1974 A theory of thermal oscillations in liquid metals. *J. Fluid Mech.* **64**, 577–588.

HART, J.E. 1972 Stability of thin non-rotating Hadley circulations. *J. Atmos. Sci.* **29**, 687–697.

HART, J.E. 1983 A note of stability of low-Prandtl-number Hadley circulations. *J. Fluid Mech.* **132**, 271–181.

HINCH, E.J. 1984 A note on the mechanism of the instability at the interface between two shearing fluids. *J. Fluid Mech.* **144**, 463–465.

HOF, B., JUEL, A., ZHAO, L., HENRY, D., BEN HADID, H. & MULLIN, T. 2004 On the onset of oscillatory convection in molten gallium. *J. Fluid Mech.* **515**, 391–413.

HU, K.X., HE, M. & CHEN, Q.S. 2016 Instability of thermocapillary liquid layers for Oldroyd-B fluid. *Phys. Fluids* **28**, 033105.

HU, K.X., HE, M., CHEN, Q.S. & LIU, R. 2017 Linear stability of thermocapillary liquid layers of a shear-thinning fluid. *Phys. Fluids* **29**, 073101.

HUERRE, P. & MONKEWITZ, P.A. 1990 Local and global instabilities in spatially developing flows. *Annu. Rev. Fluid Mech.* **22**, 173–537.

HURLE, D.T.J., JAKEMAN, E. & JOHNSON, C.P. 1974 Convective temperature oscillations in molten gallium. *J. Fluid Mech.* **64**, 565–576.

JUEL, A., MULLIN, J., BEN HADID, H. & HENRY, D. 2001 Three-dimensional free convection in molten gallium. *J. Fluid Mech.* **436**, 267–281.

KISTLER, S.F. & SCHWEIZER, P.M. 1997 *Liquid Film Coating: Scientific Principles and Their Technological Implications*. Springer.

KNOBLOCH, E. 1990 Pattern selection in long-wavelength convection. *Physica* D **41**, 450–479.

KOWAL, K.N., DAVIS, S.H. & VOORHEES, P.W. 2018 Thermocapillary instabilities in a horizontal liquid layer under partial basal slip. *J. Fluid Mech.* **855**, 839–859.

KUO, H.P. & KORPELA, S.A. 1988 Stability and finite amplitude natural convection in a shallow cavity with insulated top and bottom and heated from a side. *Phys. Fluids* **33**, 31.

KUPFER, K., BERS, A. & RAM, A.K. 1987 The cusp map in complex-frequency plane for absolute instabilities. *Phys. Fluids* **30**, 3075–3082.

LAPPA, M. 2010 *Thermal Convection: Patterns, Evolution and Stability*. Wiley.

LEVENSPIEL, O. 1999 *Chemical Reaction Engineering*. John Wiley & Sons.

MERCIER, J.F. & NORMAND, C. 1996 Buoyant-thermocapillary instabilities of differentially heated liquid layers. *Phys. Fluids* **8**, 1433.

NEPOMNYASHCHY, A.A. & SIMANOVSKII, I.B. 2004 Influence of thermocapillary effect and interfacial heat release on convective oscillations in a two-layer system. *Phys. Fluids* **16**, 1127.

NEPOMNYASHCHY, A.A. & SIMANOVSKII, I.B. 2009 Dynamics of ultra-thin two-layer films under the action of inclined temperature gradients. *J. Fluid Mech.* **631**, 165–197.

NIELD, D.A. 1994 Convection induced by an inclined temperature gradient in a shallow horizontal layer. *Intl J. Heat Fluid Flow* **15**, 157.

ORON, A. 2000 Nonlinear dynamics of three-dimensional long-wave Marangoni instability in thin liquid films. *Phys. Fluids* **12**, 1633–1645.

ORON, A. & BANKOFF, S.G. 1999 Dewetting of a heated surface by an evaporating liquid film under conjoining/disjoining pressures. *J. Colloid Interface Sci.* **218**, 152–166.

ORON, A. & GOTTLIEB, O. 2002 Nonlinear dynamics of temporally excited falling liquid films. *Phys. Fluids* **14**, 2622–2636.

ORON, A. & NEPOMNYASHCHY, A.A. 2004 Long-wavelength thermocapillary instability with the Soret effect. *Phys. Rev.* E **69**, 016313.

ORTIZ-PÉREZ, A.S. & DÁVALOS-OROZCO, L.A. 2011 Convection in a horizontal fluid layer under an inclined temperature gradient. *Phys. Fluids* **23** (8), 084107.

ORTIZ-PÉREZ, A.S. & DÁVALOS-OROZCO, L.A. 2014 Convection in a horizontal fluid layer under an inclined temperature gradient for Prandtl numbers $Pr > 1$. *Intl J. Heat Mass Transfer* **68**, 444–455.

PATNE, R., AGNON, Y. & ORON, A. 2020*a* Marangoni instability in the linear Jeffreys fluid with a deformable surface. *Phys. Rev. Fluids* **5**, 084005.

PATNE, R., AGNON, Y. & ORON, A. 2020*b* Thermocapillary instabilities in a liquid layer subjected to an oblique temperature gradient: effect of a prescribed normal temperature gradient at the substrate. *Phys. Fluids* **32**, 112109.

PATNE, R., AGNON, Y. & ORON, A. 2021*a* Thermocapillary instabilities in a liquid layer subjected to an oblique temperature gradient. *J. Fluid Mech.* **906**, A12.

PATNE, R., AGNON, Y. & ORON, A. 2021*b* Thermocapillary instability in a viscoelastic liquid layer under an imposed oblique temperature gradient. *Phys. Fluids* **33**, 012107.

SCHMID, P.J. & HENNINGSON, D.S. 2001 *Stability and Transition in Shear Flows*. Springer.

SHKLYAEV, O.E. & NEPOMNYASHCHY, A.A. 2004 Thermocapillary flows under an inclined temperature gradient. *J. Fluid Mech.* **504**, 99–132.

SMITH, M.K. & DAVIS, S.H. 1983*a* Instabilities of dynamic thermocapillary liquid layers. Part 1. Convective instabilities. *J. Fluid Mech.* **132**, 119–144.

SMITH, M.K. & DAVIS, S.H. 1983*b* Instabilities of dynamic thermocapillary liquid layers. Part 2. Surface-wave instabilities. *J. Fluid Mech.* **132**, 145–162.

SWEET, D., JAKEMAN, E. & HURLE, D.T.J. 1977 Free convection in the presence of both vertical and horizontal temperature gradients. *Phys. Fluids* **20**, 1412.

TREFETHEN, L.N. 2000 *Spectral Methods in MATLAB*. SIAM.

WALTON, I.C. 1985 The effect of a shear flow on convection near a two-dimesional hot-patch. *Q. J. Mech. Appl. Maths* **38**, 561–574.

WANG, T.-M. & KORPELA, S.A. 1989 Convection rolls in a shallow cavity heated from the side. *Phys. Fluids A* **1**, 947.

WEBER, J.E. 1973 On thermal convection between non-uniformly heated planes. *Intl J. Heat Mass Transfer* **16**, 961.

WEBER, J.E. 1978 On the stability of thermally driven shear flow heated from below. *J. Fluid Mech.* **87**, 65–84.